Pulverized granite at the brittle-ductile transition: An example from the Kellyland fault zone, eastern Maine, U.S.A.

Walter A. Sullivan[1] and Emily M. Peterman[2]

[1]Department of Geology, Colby College, 5800 Mayflower Hill, Waterville, Maine 04901, USA

[2]Department of Earth and Oceanographic Sciences, Bowdoin College, 6800 College Station, Brunswick, Maine 04011, USA

Abstract

Granite from a 50–200-m-wide damage zone adjacent to the brittle-ductile Kellyland Fault Zone contains healed fracture networks that exhibit almost all of the characteristics of dynamically pulverized rocks. Fracture networks exhibit only weak preferred orientations, are mutually cross-cutting, separate jigsaw-like interlocking fragments, and are associated with recrystallized areas likely derived from pervasively comminuted material. Fracture networks in samples with primary igneous grain shapes further indicate pulverization. Minimum fracture densities in microcline are ~100 mm/mm^2. Larger fractures in microcline and quartz are sometimes marked by neoblasts, but most fractures are optically continuous with host grains and only visible in cathodoluminescence images. Fractures in plagioclase are crystallographically controlled and typically biotite filled. Petrologic observations and cross-cutting relationships between brittle structures and mylonitic rocks show that fracturing occurred at temperatures of 400°C or more and pressures of 200 MPa. These constraints extend the known range of pulverization to much higher temperature and pressure conditions than previously thought possible. The mutually cross-cutting healed fractures also provide the first record of repeated damage in pulverized rocks. Furthermore, pulverization must have had a significant but transient effect on wall-rock

porosity, and biotite-filled fracture networks in plagioclase form weak zones that could accommodate future strain localization.

1. Introduction

The high frequency of earthquakes along modern fault zones indicates that seismogenic fault rocks should be ubiquitous in exhumed ancient faults. However, at our present level of understanding, demonstrably seismogenic fault rocks appear rather rare. The apparent paucity of seismogenic fault rocks is in part due to overprinting and recrystallization of seismogenic rocks (e.g., Passchier, 1982, Price et al, 2012; Kirkpatrick and Rowe, 2013). However, we also have historically overlooked and/or misinterpreted many fault rocks and fault structures that are likely seismogenic (see recent review in Rowe and Griffith, 2015). For example, recent mapping has identified 100–400-m-wide zones of dynamically pulverized rocks—damage-zone rocks that exhibit intense fracturing and grain-size reduction yet record no appreciable shear offset—adjacent to several large, active strike-slip fault zones, including the San Andreas Fault, the Garlock Fault, and the Arima-Takatsuki Tectonic Line (e.g., Dor et al., 2006a, 2006b, 2008, 2009; Rockwell et al., 2009; Mitchell et al., 2011).

Theoretical considerations (Reches and Dewers, 2005), rock-deformation experiments (e.g., Doan and Gary, 2009; Yuan et al., 2011; Doan and d'Hour, 2012; Aben et al., 2016), and analyses of grain-size distributions (Wilson et al., 2005; Muto et al., 2015) are all consistent with a seismogenic origin for pulverized rock. However, the exact seismic mechanism or mechanisms leading to pulverization remain equivocal (see recent review in Xu and Ben-Zion, 2017). Pulverized rocks recognized along modern fault zones exhibit little or no healing, and they commonly grade into fault cores dominated by incohesive gouge (Wilson et al., 2005; Dor et al., 2006a, 2009; Rockwell et al., 2009; Mitchell et al., 2011; Wechsler et al., 2011; Rempe et al., 2013; Muto et al., 2015). Additionally, very high-strain-rate axial compression experiments using the split Hopkinson pressure-bar apparatus fail to produce pulverization at realistic strain rates above 20 MPa confining pressures and fail to produce pulverization at any strain rate above 60 MPa (Yuan et al., 2011). These observations have led to some speculation that pulverization is only possible at very low confining pressures in the upper 2–4 km of the earthquake source region (e.g., Dor et al., 2006a; Yuan et al., 2011; Fondriest et al., 2015). Hence, constraining the maximum depth of pulverization is a critical factor in determining what seismic mechanisms may drive the process. Currently, the two most widely invoked mechanisms are rapid tensile loading on the high-seismic-velocity sides of bi-material ruptures (e.g. Ben-Zion and Shi, 2005; Dor et al., 2006a; Xu and Ben-Zion, 2017), and passing Mach fronts from super-shear ruptures (e.g. Doan and Gary, 2009; Yuan et al., 2011). Incipient pulverization textures formed at confining pressures at or below the tensile strength of quartz indicate that rapid compressional loading is also an important mechanism under at least some conditions (Whearty et al., in press).

To date, pulverized rocks have been documented only along one ancient fault zone that was exhumed from less than 2 km depth (Fondriest et al., 2015), and the potential for long-term preservation of pulverized rock is unknown. However, recognizing pulverized rocks in damage zones of ancient faults would help demonstrate seismogenic slip, and combining this paleoseismic fingerprint with careful study of adjacent fault cores could improve our understanding of the cryptic record of earthquakes in exhumed fault zones.

In this contribution we document damage-zone microstructures in granite adjacent to a bi-material interface in the Paleozoic brittle-ductile Kellyland fault zone (KFZ). Preservation of pulverization textures in the damage zone of the KFZ is significant because it: (a) extends the known range of pulverization to much higher temperatures and higher confining pressures, thereby providing some important constraints on the mechanism or mechanisms causing pulverization, and (b) shows that dynamic pulverization textures can be preserved in ancient inactive shear zones, despite complete healing in almost all grains.

2. Geologic setting

The KFZ is one of three strands of the Norumbega fault system in eastern Maine (Fig. 1). Like the San Andreas fault system, the Norumbega system formed parallel with a long-lived active margin (e.g., Hatcher, 2010), cuts many arc- and oceanic-affinity accreted terranes as well as plutonic rocks (e.g., Robinson et al., 1998; Ludman and West, 1999; Hibbard et al., 2006), and offsets the seismic Moho (Costain et al., 1990; Doll et al., 1996). Regional mapping and palenspastic reconstructions indicate that the KFZ accommodated at least 25 km of dextral strike-slip motion (Wang and Ludman, 2004). In the area of this study, the KFZ forms a bi-material interface juxtaposing chlorite-grade metasedimentary rocks of the Flume Ridge Formation with the ca. 384-Ma Deblois granite pluton (Fig. 1) (Wang and Ludman, 2004; Wang, 2007). The Deblois pluton has a 0.5–1-km-wide contact areole (Ludman et al., 2000; Riley, 2004), and U-Pb-crystallization- and biotite-^{40}Ar/^{39}Ar-cooling ages of granite collected near the study area are within error of each other (Idleman and Ludman 1998; Ludman et al., 1999; Ludman et al., 2000), indicating rapid cooling and shallow emplacement.

Sullivan et al. (2013) recognized three strain facies in the KFZ cutting the Deblois granite. From southeast to northwest these are: (1) a 2–3-km-wide belt of variably foliated to undeformed granite called the foliated-granite domain, (2) a 100–300-m-wide belt of foliated-granite cut by numerous small shear zones called the localized-shear-zone domain, and (3) a 200–400-m-wide belt of ultramylonite and minor mylonite derived from granite called the main-ultramylonite domain (Fig. 1B). Bulk composition does not change between undeformed granite, foliated-granite, and granite-derived ultramylonite (Sullivan et al., 2013).

Undeformed Deblois granite is texturally uniform and megacrystic to pegmatitic. It contains perthitic microcline + quartz + oligoclase + biotite + hornblende; rapakivi overgrowths of plagioclase on microcline are common (Riley, 2004; Wang, 2007). The foliated-granite domain is marked by aligned feldspar megacrysts and weakly elongated quartz and biotite grains, but many areas of this domain do not exhibit foliation. Quartz in this domain underwent fast grain-boundary-migration recrystallization and often preserves chessboard-style subgrains indicating high-temperature deformation (>600°C; Kruhl, 1996; Stipp et al., 2002; Sullivan et al., 2013).

The localized-shear-zone domain consists of foliated-granite cut by numerous, discrete, 2-mm- to 1.5-m-wide steeply dipping mylonite and ultramylonite zones (Fig. 2A). Most shear zones are bounded by at least one discrete fracture surface. These boundaries truncate wall-rock foliations and individual mineral grains. Both synthetic and antithetic discrete brittle fractures also cut the foliated granite, and many antithetic fractures root into localized shear zones where they exhibit synthetic drag (Sullivan et al., 2013). Localized shear zones where foliation planes are cut by brittle fractures have not been documented, but foliation in localized shear zones sometimes bends around offset shear-zone boundaries. Sharp shear-zone boundaries locally transition into discrete fractures. Probable recrystallized and deformed pseudotachylyte veins are preserved in some localized shear zones (Sullivan et al., 2013). The ubiquitous association of shear zones with fractures, the presence of recrystallized and deformed brittle fault rocks, and the composition and textures of mylonites and ultramylonites described by Sullivan et al. (2013) indicate that ductile deformation in the localized shear zones was catalyzed by grain-size reduction and mechanical mixing during brittle faulting. The localized-shear-zone domain grades into the main-ultramylonite domain over 2–10 m (Fig. 1B). Granite-derived ultramylonite does not contain brittle fractures like those observed in the localized-shear-zone domain.

3. Criteria for identifying pulverized rocks

Samples of pulverized crystalline rock collected adjacent to modern fault zones exhibit a characteristic suite of microstructural features that may be used to recognize ancient pulverized rocks. These are: (a) primary grain shapes are preserved despite pervasive fracturing; (b) dilational, opening-mode fractures are common; (c) primary quartz and feldspar grains host zones of intensely comminuted material; (d) fracture sets have little or no preferred orientation and form jigsaw-like interlocking fragments; (e) fractures typically do not offset primary structures; and (f) there is little or no rotation of fragments across most fractures (c.f. Mitchell et al., 2011; Wechsler et al., 2011; Rempe et al., 2013). These textures are typically gradational with gouge and cataclasite in the fault core and intact rock outside of the damage zone (Dor et al., 2006a, 2006b; Rockwell et al., 2009; Mitchell et al., 2011; Wechsler et al., 2011; Rempe et al., 2013). Both experiments and observations of natural fault rocks indicate that healing of fractures is rapid at temperatures typical of the brittle-ductile transition with smaller fractures often healed in crystallographic continuity with their host grains (e.g., Küster et al., 2001; Trepmann et al., 2007; Anders et al., 2014; Bestmann et al., 2016). Thus, repeated seismogenic pulverization at elevated temperatures should produce multiple generations of opening-mode fractures that cut healed fractures from earlier events.

Cataclasites, dynamic dilational breccias, and implosion breccias are also associated with intense fracturing and grain-size reduction in or adjacent to large brittle-ductile fault zones. However, each of these fault rocks can be distinguished from end-member dynamically pulverized rock. Cataclasites exhibit offset and rotation of fragments, disaggregation of primary textures, and through-going bands of fine-grained material (e.g., Sibson, 1977; Evans, 1988; Blenkinsop, 1991; Nelis and Mosher, 1998). Fracturing and cataclasis of feldspars is considered common in granite deformed under greenschist-facies conditions (e.g., Simpson, 1985; Tullis and Yund, 1987), but formation of these fractures is associated with mesoscopic deformation of the feldspar grains, foliation formation, and crystal-plastic deformation of quartz and biotite (e.g., Simpson, 1985; Gapais, 1989; Tullis, 2002). Dynamic dilational breccias exhibit crackle to mosaic textures with strong fracture preferred orientations and contain mesoscopic clasts (Melosh et al., 2014). Implosion breccias are restricted to dilational sites, typically contain mesoscopic clasts, and host many veins (Sibson, 1986).

4. Methods

We examined granite specimens from throughout the localized-shear-zone domain and adjacent foliated-granite domain and one granite sample collected ~4.9 km from the KFZ. To minimize the complications of fracturing related to foliation development and/or overprinting by later deformation, we focused our analyses on localities with no mesoscopic foliation or only weak mesoscopic foliations. Polished thin sections of each sample were initially characterized with a transmitted-light microscope and then carbon coated and analyzed using a Tescan Vega3 scanning electron microscope equipped with a Tescan color cathodoluminescence (CL) detector housed at Bowdoin College. The Color-CL detector can be operated in panchromatic-CL or color-CL mode; in color-CL mode, dichroic filters are used to measure the light emitted within red, green, and blue wavelengths to produce a color image. Color-CL and backscattered-electron (BSE) images were collected from the same fields of view to assist in phase identification. Color-CL images were collected using a working distance of 15 mm and accelerating voltages of 18–20 kV for quartz and 18 kV for microcline and plagioclase. Because CL intensity varied among grains within and across samples, contrast and brightness settings were optimized to highlight variations in CL intensity within each grain. Thus, CL colors and CL intensity cannot be directly compared among images.

Fracture maps of microcline grains were generated by tracing overlaid color-CL and BSE images in Adobe Illustrator. Plagioclase in our samples has much lower CL intensities than microcline, but similar CL colors. Hence, it was sometimes difficult to distinguish healed fractures from long, thin perthitic exsolution lamellae. In these cases we did not digitize questionable fracture/lamellae traces. It was also impossible to trace all fractures across large exsolution lamellae or plagioclase inclusions, and fractures often could not be traced across dark zones of recrystallized K-feldspar. Individual fractures were traced using successive straight-line segments that approximate the curvature and irregularities of each fracture. Fracture-orientation measurements were compiled from a unit circle in the center of each image. Fracture traces were converted to a series of nodes in XY-coordinate space, and the orientation of each straight-line segment was measured in sample coordinates using the MATLAB toolbox FracPaQ (Healy et al., 2017). This method accounts for the nonlinearity of the fractures and gives more weight to longer fractures that typically contain more line segments (Griffith et al., 2010; Healy et al., 2017). Compiled fracture orientations are plotted on Rose diagrams with each sector proportional to the frequency of orientations. As far as we are aware, FracPaQ does not calculate average fracture densities for entire fracture maps or report the total length of fracture segments. Therefore, average fracture densities were compiled by multiplying the total number of segments by the average segment length in mm to obtain the total fracture length and then dividing by the area of the inventory circle in mm^2. We interpret these as minimum density measurements because fractures in some parts of each grain could not be mapped.

5. Results

5.1. Station KL40

5.1.1. Sample KL40-2B

Station KL40 is a 1-m^2 pavement outcrop of granite traversed by a 5–10-cm-wide, northeast-striking, dextral mylonite/ultramylonite zone (Figs. 1B, 2) (Sullivan et al., 2013; their Figures. 6C, 8). Sample KL40-2B spans the abrupt boundary between granite and the mylonite/ultramylonite zone (Figs. 2A, 3A). Granite in KL40-2B is also traversed by a north-northwest-striking sinistral transgranular shear fracture that offsets the edge of the mylonite/ultramylonite zone but is deformed by it, and mylonitic fabrics grade into highly fragmented quartz grains on one side of this shear fracture (Fig. 3A). Ultramylonite matrix in this sample is biotite rich and quartz poor relative to the granite protolith (Sullivan et al., 2013), which is consistent with disequilibrium melting (Spray, 2010). The composition and the geometry of ultramylonite bands in the shear zone indicate that ultramylonite formed after pseudotachylyte.

Primary quartz domains in the granite of KL40-2B are divided into 0.5–3.5-mm-wide, irregularly shaped to amoeboid grains that exhibit sweeping and/or patchy undulose extinction. Boundaries of these grains are typically decorated with 5–20-μm-wide serrations and irregular zones of 5–25-μm-wide neoblasts. All quartz grains are traversed by 10–50-μm-wide, planar or curviplanar bands of 5–25-μm-wide quartz neoblasts and, locally, biotite that often cut quartz-quartz and quartz-feldspar grain boundaries (Fig. 3B). Some grains also host irregularly shaped zones of neoblasts that merge with the thin bands. These bands and irregular zones of neoblasts resemble quartz microstructures formed by low-stress recrystallization after transient high-stress crystal-plastic deformation and intragranular microfracturing (Trepmann et al., 2007; Trepmann and Stöckert, 2013; Trepmann et al., 2017). At least some curviplanar bands of neoblasts must be healed transgranular fractures because they cut quartz-quartz and quartz-feldspar grain boundaries and/or contain biotite that requires a pathway for solution transfer. Close association of neoblast bands with the larger shear fracture in this sample (Fig. 3B) also supports a healed-fracture origin for these microstructures. Both large quartz grains and neoblasts in this sample are CL-dark in panchromatic-CL and color-CL images. Quartz formed under typical magmatic conditions is usually CL-bright because of high concentrations of Ti (Spear and Wark, 2009; Leeman et al., 2012; Mills et al., 2017; see also Götze et al., 2001).

However, deformed or recrystallized quartz yields comparatively lower CL intensity, in part due to lower Ti solubility in quartz with decreasing temperature and increasing lattice strain (Wark and Watson, 2006; Ashley et al., 2014; see discussions in Thomas et al., 2010, 2015; Huang and Audétat, 2012). Therefore, CL-dark domains within quartz are consistent with recrystallization of damaged material at relatively low temperatures.

The single large primary microcline grain in KL40-2B exhibits patchy undulose extinction in cross-polarized light, but the entire grain goes extinct within 5–10° of stage rotation indicating little net rotation between extinction domains (Figs. 3A, B). This grain is dissected by optically visible healed fractures marked by 10–50-μm-wide, planar to curviplanar bands of finely recrystallized K-feldspar ± quartz ± biotite (Fig. 3B). Some of these fractures visibly offset grain boundaries and/or perthitic lamellae whereas others show no visible offset. Most optically visible fractures form the boundaries of extinction domains. Color-CL images of optically continuous microcline reveal jigsaw-like networks of CL-bright feldspar separated by 2–100-μm-wide bands and zones of CL-dark material that pervasively disrupt perthitic lamellae and primary inclusions (Figs. 3C–E). Bands of CL-dark material are planar to curviplanar, commonly branch, and are mutually cross-cutting in all directions (Figs. 3C, E). Based on these geometries and clear cross-cutting relationships with primary features, we interpret CL-dark bands as healed fractures. Most fractures exhibit no offset, and many are dilational (Fig. 3D). Dilational fractures are primarily filled with K-feldspar variably intergrown with quartz and biotite (Fig. 3E), but some areas are quartz or biotite dominated. Zones of CL-dark material are semi-polygonal to amoeboid in shape, often taper into healed fractures, often have fractures radiating from them in many directions, and often host island grains of higher-luminosity material (Figs. 3C, E). CL-dark zones with radiating fractures and CL-bright islands likely represent pervasively comminuted domains that were largely recrystallized upon healing, but a few semi-polygonal zones could be dilational jogs along shear fractures. Fracture trends span a full 180° in sample coordinates, but they do define a slight preferred orientation with the maximum fracture densities roughly bisecting the obtuse angle between the faults in this sample, as expected for wing cracks or extension fractures (Fig. 3D). The average fracture density in this sample is 118 mm/mm^2 or 1.18×10^5 m/m^2 (Table 1).

5.1.2. Sample KL40-8

KL40-8 is a non-oriented sample of granite collected ~35 cm across strike from the mylonite/ultramylonite zone (Fig. 2). It is traversed by a shear fracture with 1–2 mm of apparent dextral separation, but the outlines of primary grains, igneous zoning, and igneous inclusions are preserved (Fig. 4A). Primary quartz domains in KL40-8 are divided into 0.5–4-mm-wide, semi-polygonal to amoeboid grains with sweeping and/or patchy undulose extinction. Quartz grain boundaries exhibit the same serrated edges and zones of neoblasts observed in KL40-2B, and quartz grains are also traversed by thin bands of neoblasts that often merge with irregular zones of neoblasts hosted in larger grains or mantling smaller grains (Fig. 4B). Color-CL images of quartz reveal a highly irregular patchwork of CL-dark and bright material (Fig. 4C). CL-bright domains are traversed by many 2–30-μm-wide, planar to curviplanar bands of CL-dark quartz interpreted as healed fractures—consistent with previous interpretations of instantaneously healed microfractures in quartz (Bestmann et al., 2016). Most of these healed fractures are crystallographically continuous with the host grain and are not visible in cross-polarized light. Fractures are mutually cross-cutting, and often can be correlated or traced across larger CL-dark domains (Fig. 4C). The patchwork of CL-bright and CL-dark quartz obscures many fractures, so we did not attempt to map them.

Primary microcline grains in KL40-8 exhibit patchy to sweeping undulose extinction in cross-polarized light with entire grains going extinct in 5–10° of stage rotation indicating little net rotation between extinction domains (Fig. 4A). They also host optically visible, mutually cross-cutting healed fractures marked by 10–100-μm-wide, planar or curviplanar bands of finely recrystallized K-feldspar ± quartz ± biotite. As in KL40-2B, some of the larger fractures offset grain boundaries and form the boundaries of extinction domains. However, most fractures exhibit no offset or rotation. A color-CL map of the microcline grain in the lower right-hand side of Figure 4A reveals nearly intact oscillatory zoning. High-magnification color-CL images of optically continuous microcline reveal jigsaw-like networks of fragments separated by mutually cross-cutting, healed fractures and zones of recrystallized material (Fig. 4E–H). Many of these fractures also are dilational and filled with K-feldspar variably intergrown with quartz and biotite (Fig. 4G). Fracture trends in two microcline grains of KL40-8 span a full 180°, but they also define one or two weak preferred orientations. The dominant preferred orientation in both grains is inclined at ~60° anti-clockwise to the shear fracture bisecting the sample (Figs. 4F, H)—opposite what is expected for wing cracks or extension fractures related to the fault. One grain also exhibits a second weak preferred orientation inclined ~25–30° clockwise to the shear fracture (Fig. 4F). Average fracture densities in this sample are similar to KL40-2B (Table 1). Plagioclase grains in KL40-8 are dissected by polygonal networks of dilational fractures primarily filled with finely recrystallized biotite (Fig. 4D). These fractures typically follow albite-twin and cleavage planes. There is little difference in extinction angle across most fractures indicating little or no rotation or offset. Biotite-filled fractures in plagioclase locally transition into quartz- or microcline-filled fractures in neighboring quartz or microcline grains.

5.2. Elsewhere in the localized-shear-zone domain

Two foliated granite samples, KL115 and KL109-B, were collected 20 m along strike from each other 3.15 km northeast of station KL40 in the localized-shear-zone domain (Fig. 1B). Weak mesoscopic foliations in these rocks are defined by elongated quartz and biotite grains and rotated and aligned tabular feldspar grains. Cross-polarized-light and color-CL images of quartz in KL115 and KL109-B exhibit the same microstructures observed in KL40-8. One primary quartz grain observed in KL115 is drawn into a ribbon with a distinct core-mantle recrystallization texture defined by bands of 5–30-μm-wide neoblasts surrounding elongated relict grains. Relict grains and bands of neoblasts correspond to CL-dark and CL-bright domains in color-CL images, and the CL-bright relict grains are locally cut by healed fractures. Microcline grains observed in color-CL images exhibit jigsaw-like networks of fragments separated by 5–100-μm-wide healed fractures and many zones of recrystallized material that commonly have fractures radiating from them (Fig. 5). Fracture fill is identical to that in KL40-8. Dilational fractures in KL115 are primarily perpendicular to the mesoscopic foliation whereas those in KL109-B are both perpendicular to and parallel with the foliation. Fracture populations in both samples span a full 180°, but they also exhibit weak preferred orientations either perpendicular to (KL115) or parallel with (KL109-B) foliation. Average fracture densities in KL115 and KL109-B are similar to those in samples from station KL40 (Table 1). Plagioclase in these samples also exhibits networks of crystallographically controlled biotite-filled fractures. A single foliated-granite sample collected from the localized-shear-zone domain at station KL13, 3.57 km southwest of KL40 (Fig. 1B), exhibits similar healed fractures and biotite-filled-fracture networks in cross-polarized-light and BSE images, but this sample was not examined using color-CL.

Outcrops of granite in the localized-shear-zone domain almost universally exhibit a characteristic weathering pattern wherein microcline disaggregates randomly producing very irregular surfaces at the mm to cm scale (Fig. 2B). This weathering pattern exists regardless of whether or not the granite is foliated, and it is almost certainly a result of the pervasive microfracturing of microcline in these rocks. In contrast, microcline grains in foliated and undeformed granite exposed outside of the localized-shear-zone domain disaggregate along systematic fractures and/or cleavage surfaces producing more regular, blocky weathering surfaces at the mm to cm scale (Fig. 2C).

5.3. Samples outside of the localized-shear-zone domain

We examined four granite samples collected at sites KL51, KL41, KL110, and KL111 outside of the localized-shear-zone domain (Fig. 1B). Site KL51 is outside of the foliated-granite domain 4.9 km across strike from the KFZ (see Figure 2 of Sullivan and Monz, 2013 for exact location), and granite here exhibits a primary igneous texture in outcrop and thin section (Fig. 6A). Quartz domains consist of polycrystalline aggregates of 0.5–3.5-mm-wide irregularly shaped to semipolygonal grains. Quartz-quartz grain boundaries are curviplanar to irregular in shape and commonly exhibit many 100–400-μm-wide lobate indentations. Individual quartz grains all go extinct within 5° of stage rotation, but some grains exhibit 100–400-μm-wide polygonal subgrains. Most quartz grains contain planar inclusion trails that often cross grain boundaries. However, there are no curviplanar bands or irregular zones of neoblasts as observed in samples from the localized-shear-zone domain, and CL images of quartz grains in sample KL51 exhibit none of the planar to curviplanar CL-dark bands or irregular zones of CL-dark material seen in samples from the localized-shear-zone domain (Fig. 6B). Microcline from KL51 commonly exhibits tartan twinning and ubiquitously hosts vermiform perthitic exsolution lamellae (Figs. 6C, D). Exsolution lamellae and twinning create a complex mosaic of bright and less-bright areas in color-CL images (Fig. 6D), but microcline grains from this site exhibit none of the evidence for fracturing seen in localized-shear-zone-domain samples such as planar to curviplanar trails of neoblasts or bands of CL-dark material cutting primary features.

Site KL41 is ~150 m across strike from KL40. In hand sample, granite at KL41 exhibits a primary igneous texture (Fig. 7A). Most primary quartz domains in sample KL41 are divided into 0.25–5-mm-wide, semi-polygonal to amoeboid grains with sweeping undulose extinction (Fig. 7B). Quartz-quartz grain boundaries are typically decorated with 5–20-μm-wide serrations ± neoblasts, but thin bands and irregular zones of neoblasts are much less common than in localized-shear-zone-domain samples. Color-CL images of primary quartz bodies reveal a patchwork of irregularly shaped, high-luminosity domains surrounded by zones of CL-dark material hosting small CL-bright islands (Fig. 7C). CL-bright quartz domains contain mutually cross-cutting, planar-systematic sets of healed fractures, but these fractures typically cannot be traced across CL-dark bands. Color-CL images of relatively intact primary quartz bodies such as the one visible in the right-hand side of Figure 7B reveal very few fractures and areas of CL-dark material. The patchworks of CL-dark and CL-bright material along with local patchy undulose extinction are also consistent with partial static recrystallization of quartz driven by intra-crystalline damage developed during transient high-stress deformation (Trepmann et al., 2017). Microcline in KL41 exhibits straight or sweeping undulose extinction, and perthitic lamellae are largely intact (Fig. 7B). Color-CL images of these grains reveal sets of planar-systematic fractures cutting primary features and a few irregularly shaped, CL-dark domains (Fig. 7D). Fracture sets are mutually cross cutting, exhibit no shear offset, and are locally dilational (Fig. 7D). Overall fracture density is also very low compared to samples from the localized-shear-zone domain. Some primary plagioclase grains in KL41 host polygonal networks of biotite-filled fractures identical to those observed in localized-shear-zone-domain samples, but others remain intact.

Sites KL110 and KL111 are ~36 and ~121 m across strike from KL115 respectively (Fig. 1B). Granite at both sites exhibits a mesoscopic foliation defined by elongated quartz grains and rotated and aligned tabular feldspar grains. Granite at KL110 also exhibits type-I S-C fabrics (Lister and Snoke, 1984) with C surfaces defined by ribbons of quartz and biotite. Quartz domains in samples KL110 and KL111 are dominated by 10–80-μm-wide, semi-polygonal neoblasts (Fig. 7F). Sparse relict grains within recrystallized quartz bands exhibit subgrains the same size and shape as neoblasts. These microstructures indicate subgrain-rotation recrystallization (e.g., Hirth and Tullis, 1992; Stipp et al., 2002). Healed fractures are locally visible in relict quartz grains (Fig. 7F), but not visible in neoblasts. Microcline grains in these samples exhibit straight or sweeping undulose extinction, and some grains host 20–100-μm-wide, foliation-perpendicular dilational fractures marked by bands of 5–20-μm-wide K-feldspar ± quartz ± plagioclase ± biotite neoblasts (Fig. 7E). Color-CL images of microcline reveal single sets of planar-systematic fractures that are roughly parallel with or perpendicular to the foliation (Fig. 7G), and overall fracture density is very low compared with KL115 and KL109-B.

6. Discussion

6.1. Temperature and pressure conditions during fracturing

A variety of structural and petrologic observations provide constraints on the conditions of fracturing in our samples. Cross-cutting relationships between the brittle fractures and the mylonitic fabric observed in KL40-2B and elsewhere in the localized-shear-zone domain show that brittle deformation was coeval with or predated mylonitic deformation and therefore must have formed at the granite brittle-ductile transition. Quartz ribbons in granite-derived mylonitic rocks of the KFZ underwent subgrain-rotation dynamic recrystallization during dislocation creep and record flow stresses of 80–130 MPa (Sullivan et al., 2013; Sullivan and Monz, 2016). These flow-stress values indicate relatively high strain rates (e.g., Gleason and Tullis, 1995; Hirth et al., 2001), and dominance of subgrain-rotation recrystallization at relatively high strain rates indicates deformation temperatures of 400 °C or more (Stipp et al., 2002). Additionally, biotite is the only stable sheet silicate in healed fractures and the only stable sheet silicate in Fe-rich, Si-depleted ultramylonite matrix throughout the localized-shear-zone domain (Sullivan et al., 2013). Pelites deformed by the KFZ across strike from the study area also contain prograde biotite that was in equilibrium with calcite-buffered fluids (Sullivan and Monz, 2016). Hence, fracturing must have occurred in the biotite stability field, and this also indicates temperatures in excess of 400°C (e.g., Spear and Cheney, 1989; Spear, 1993).

There are no direct estimates of confining pressure from the KFZ, but flow stresses recorded by mylonitic rocks and metamorphic mineral assemblages provide some pressure constraints. Flow stresses recorded by dynamically recrystallized quartz aggregates at the brittle-ductile transition should be significantly less than peak differential stresses achieved prior to brittle failure (e.g. Trepmann and Stöckert, 2003; Handy and Brun, 2004; Trepmann et al., 2017). Therefore, effective confining pressures during episodes of brittle deformation along the brittle-ductile KFZ must have been high enough to support differential stresses well in excess of 100 MPa. Rapid cooling of the Deblois granite combined with progressive overprinting of high-temperature microstructures by low-temperature microstructures requires that the KFZ formed almost immediately after crystallization of the granite (Wang and Ludman, 2004; Sullivan et al., 2013). Thus, the crystallization pressure of the granite is a good approximation of the confining pressure during fault movement and fracturing. Unfortunately, quantitative pressure-temperature estimates for the Deblois granite and/or rocks in its contact areole have not been published. However, pelites of the Flume Ridge Formation in the contact areole of the Deblois granite locally contain sillimanite (Riley, 2004). Sillimanite is not stable below 200 MPa pressure until after the Al_2SiO_5 + K-feldspar isograd is crossed (Holdaway, 1971; Spear and Cheney, 1989), and it may not be stable at pressures below 200 MPa until after the wet-granite solidus is crossed (Pattison, 1992). There is no evidence that sillimanite-bearing Flume Ridge Formation samples reached the Al_2SiO_5 + K-feldspar isograd, let alone the wet-granite solidus. Hence, sillimanite in the contact areole of the Deblois granite indicates metamorphic pressures of 200 MPa or more. Wang and Ludmann (2004) also inferred metamorphic pressures of about 200 MPa in this area based on regional chlorite-grade metamorphism of rocks intruded by the Deblois pluton.

6.2. Fracture-forming mechanism

The pervasively fractured granite samples from the localized-shear-zone domain exhibit all of the characteristics common to pulverized granite in the upper crust including: (a) primary grain shapes are preserved despite multiple generations of fracturing and healing; (b) dilational, opening-mode fractures are common; (c) irregular recrystallized zones likely derived from intensely comminuted material are hosted in primary microcline grains; (d) fracture sets have little preferred orientation and form jigsaw-like interlocking fragments; (e) fractures typically do not offset primary structures or earlier healed fractures; and (f) there is little or no rotation of fragments across most fractures (c.f. Mitchell et al., 2011; Wechsler et al., 2011; Rempe et al., 2013). None of these features are present at site KL51, 4.9 km across strike from the KFZ. Microcline in foliated-granite samples from outside of the localized-shear-zone domain does exhibit microfractures, but these form planar-systematic sets with much lower overall fracture densities. Our samples also do not exhibit: (a) the offset and rotation, disaggregation of primary textures, and through-going bands of fine-grained material common to cataclasites (e.g., Sibson, 1977; Evans, 1988; Blenkinsop, 1991; Nelis and Mosher, 1998); (b) the crackle to mosaic textures with strong fracture preferred orientations common to dynamic tensional breccias (Melosh et al., 2014); or (c) veins and mesoscopic clasts common to implosion breccias (Sibson, 1986). Microfracturing in the localized-shear-zone domain also is not restricted to obvious dilational sites. We are aware of no measurements of fracture density from upper crustal pulverized rocks. However, three tonalite samples from the San Jacinto fault containing fracture networks interpreted as incipient pulverization texture exhibit fracture densities that are 10–25% of our minimum fracture-density measurements (Whearty et al., in press). The crystallographic control of fractures in plagioclase in our samples is also observed in pulverized rocks from the upper crust (Wechsler et al., 2011). The only published quantitative analysis of fracture orientations in pulverized granite (Rempé et al., 2013) documented weak preferred orientations of fractures in some samples. These are similar to the preferred orientations in microcline in samples KL40-8, KL115, and KL109-B. The systematic relationship between fracture orientations and foliation in KL115 and KL109-B indicates that fracturing in these samples may be partly related to foliation development or that foliation development might have modified fractures after they formed. However, the pattern and density of fractures does not match foliated-granite samples from outside the localized-shear-zone domain. Additionally, the irregularly shaped zones of pervasively comminuted material with radiating fractures in both samples and the foliation-parallel dilational fractures in KL109-B indicate that at least some fracturing in KL115 and KL109-B records pulverization. Granite sampled at KL40 has no foliation and preserves primary igneous grain shapes, so fracturing in KL40-2B and KL40-8 cannot be related to foliation development. Preferred orientations of fractures in KL40-8 also are not obviously related to the shear fracture traversing the sample. Therefore, pulverization is the most likely mechanism to explain the pervasive fracture networks in KL40-8. Additionally, quartz typically deforms plastically in the biotite stability field at long-term geologic strain rates (e.g., White, 1976; Stipp et al., 2002). Pervasive fracturing of quartz in our samples requires strain rates at least two or three orders of magnitude faster than long-term geologic rates (e.g., Hirth and Tullis, 1994; Stipp et al., 2002; Bestmann et al., 2016). The low bulk strains in these samples further require that high strain rates were transient, and transient high strain rates are a fingerprint of the seismic cycle (e.g., Handy and Brun, 2004). The bands and irregular zones of quartz neoblasts also indicate healing after transient high-stress deformation (Trepmann et al., 2017). Finally, the occurrence of recrystallized pseudotachylyte in the localized-shear-zone domain independently confirms that seismogenic faulting occurred at this structural level in the KFZ. Based on these observations and arguments, we interpret networks of healed fractures in the granite of the localized-shear-zone domain as a fingerprint of dynamic pulverization at the granite brittle-ductile transition. The mm- to cm-scale irregular weathering pattern of pervasively fractured microcline (Fig. 2B) is nearly ubiquitous in the localized-shear-zone domain, and rocks exhibiting this weathering pattern likely underwent the same fracturing observed in our isolated samples. Thus, granite of the localized-shear-zone domain probably represents a 50–200-m-wide belt of pervasive pulverization adjacent to the KFZ throughout the area of this study (Fig. 1; see also Figure 2 of Sullivan et al., 2013).

6.3. Broader implications

Our results show that the mechanism or mechanisms causing pulverization over large areas must extend to the brittle-ductile transition at temperatures and confining pressures of at least 400 °C and 200 MPa. This contradicts experimental results where pulverization under rapid compression is not possible above 60 MPa confining pressure (Yuan et al., 2011). However, the microstructure of pulverized rocks indicates they form in response to tension rather than compression (Mitchell et al., 2011; Wechsler et al., 2011; Rempe et al., 2013; Xu and Ben-Zion, 2017). Rocks are much weaker under dynamic tension than dynamic compression (Zhang and Zhao, 2014; Xia and Yao, 2015), and numerical models of crack propagation indicate fractures will have no preferred orientation under isotropic tension (tension in all directions) (Daphalapurkar et al., 2011). Therefore, dynamic isotropic tension is the most likely mechanism for forming pulverized rock under high confining pressures (Xu and Ben-Zion, 2017). Two-dimensional numerical models of off-fault stress fluctuations around bi-material ruptures at confining pressures of 50 MPa indicate that large earthquakes can generate significant off-fault damage and transient isotropic tension 100 m or more from the fault (Ben-Zion and Shi, 2005; Xu and Ben-Zion, 2017). Bi-material ruptures involving sub-Rayleigh-to-supershear transitions (mother-daughter transitions) may produce trailing seismic pulses with even greater magnitudes of isotropic tension (Xu and Ben-Zion, 2017). The KFZ in the area of this study does form a bi-material interface between granite and low-grade metasedimentary rocks (Fig. 1), and we tentatively invoke pulses of isotropic tension generated by bi-material ruptures to explain pulverization of granite in the study area. Dynamic stress concentration and tensile pulses along bi-material ruptures are theoretically confined to the side of the fault with higher seismic velocities, and off-fault damage and pulverization should be much less extensive on the low-velocity side of the fault (Ben-Zion and Shi, 2005; Xu and Ben-Zion, 2017). Unfortunately, there is very little outcrop on the northwest side of the KFZ, and detailed mapping has revealed no outcrops of metasedimentary rocks within 200 m of the shear zone (Wang, 2007; Sullivan and Monz, 2016), so, we cannot test this prediction.

Elevated pore-fluid pressure may also enable pulverization at greater depths. There is abundant evidence for persistent elevated pore-fluid pressure in metasedimentary rocks cut by the KFZ including multiple generations of synkinematic veins and pressure-shadow overgrowths on porphyroclasts (Sullivan and Monz, 2016). However, these features are absent in foliated-granite and granite-derived mylonitic rocks on the southwest side of the fault (Sullivan et al., 2013). The absence of extensive mineral deposition in dilational sites in fault rocks derived from Deblois granite indicates that pore-fluid pressures were well below lithostatic pressures during deformation. Additionally, elevated pore-fluid pressures should weaken grain boundaries during dynamic tension, but it is unlikely that pore-fluid pressure would weaken fluid-free grain interiors under dynamic tension and promote the extensive intragranular fracturing in our samples. Hence, we are wary of invoking pore-fluid pressure to help explain pulverization adjacent to the KFZ.

The completely healed fractures in our samples also enable some important conclusions. First, the multiple generations of cross-cutting healed fractures provide the first direct record of successive fracturing events in pulverized rocks. This record confirms that repeated loading can be an important part of the pulverization process as indicated by experiments and theoretical considerations (Doan and D'Hour, 2012; Aben et al., 2016). Second, fractures in microcline and quartz are primarily healed with their host mineral. This healing should return fractured microcline and quartz grains to nearly their original strength. However, fractures in plagioclase are primarily filled with biotite, creating mosaics of smaller feldspar grains surrounded by biotite that can serve as sites for future strain localization. Finally, at least some fractures in all phases are healed with phase mixtures or exotic phases. This indicates significant grain-scale diffusive mass transfer occurred after fracturing and that the fractures greatly enhanced grain-scale wall-rock permeability; however, enhanced permeability must have been transient because of the healing process.

7. Conclusions

Granite samples from a 50–200-m-wide damage zone adjacent to the main strand of the Paleozoic strike-slip KFZ contain dense networks of healed fractures that exhibit almost all of the characteristics common to pulverized rocks in the upper crust. Fractures in this zone exhibit only weak preferred orientations, are often dilational, are mutually cross-cutting, separate jigsaw-like interlocking fragments, are often intimately associated with large recrystallized areas likely derived from pervasively comminuted material, and rarely offset primary structures. Minimum fracture densities in microcline grains are ~100 mm/mm^2 or 10^5 m/m^2. Larger fractures in microcline and quartz are sometimes marked by bands of neoblasts, but most fractures in these minerals are optically continuous with their host grains and only visible in CL images. Fractures in plagioclase are crystallographically controlled and typically filled with biotite. Microstructural and petrologic observations and cross-cutting relationships between fracture networks, brittle faults, and small mylonitic shear zones show that fracturing occurred at the granite brittle-ductile transition under temperatures of 400°C or more and confining pressures of 200 MPa. Fracture networks are found in weakly foliated *and* non-foliated-granite within the field area; the presence of fracture networks in samples that exhibit no foliation or other evidence for pervasive cataclastic shearing further indicates that granite in this damage zone records dynamic pulverization. These observations extend the known range of dynamic pulverization to much higher temperature and pressure conditions than previously thought possible, and this favors a dynamic tension mechanism for pulverization. The mutually cross-cutting healed fractures in pulverized granite also provide the first direct record of repeated loading and damage in pulverized rocks. Furthermore, pulverization in this zone must have had a significant but transient effect on grain-scale wall-rock porosity, and the biotite-filled fracture networks in plagioclase may also form weak zones able to accommodate future strain localization.

Acknowledgements

This work was funded by the Colby College Natural Science Division and NSF MRI 1530963 to Peterman. Although we ultimately used a different platform, we wish to thank W. A. Griffith for sharing a computer program for fracture analysis. C. D. Rowe also provided helpful advice on interpreting microstructures and recognizing recrystallized pseudotachylyte. The final version of this manuscript was improved by reviews from W. A. Griffith and an anonymous reviewer, but any remaining errors are our own.

References cited

Aben, F. M., Doan, M.-L., Gratier, J. P., Renard, F., 2017. High strain rate deformation of porous sandstone and the asymmetry of earthquake damage in shallow fault zones. Earth and Planetary Science Letters 463, 81–91.

Aben, F. M., Doan, M.-L., Mitchell, T. M., Toussaint, R., Reuschlé, T. Fondriest, M., Gratier, J. P., Renard, F., 2016. Dynamic fracturing by successive coseismic loadings leads to pulverization in active fault zones. Journal of Geophysical Research: Solid Earth 121, 2338–2360, doi:10.1002/2015JB012542.

Anders, M. H., Laubach, S. E., Scholz, C. H., 2014. Microfractures: A review. Journal of Structural Geology 69 part B, 377–394.

Ashley, K. T., Carlson, W. D., Law, R. D., Tracy, R. J., 2014. Ti resetting in quartz during dynamic recrystallization: Mechanisms and significance. American Mineralogist 99, 2025–2030.

Ben-Zion, Y., Shi, Z., 2005. Dynamic rupture on a material interface with spontaneous generation of plastic strain in the bulk. Earth and Planetary Science Letters 236, 486–496.

Blenkinsop, T. G., 1991. Cataclasis and processes of particle size reduction. Pure and Applied Geophysics 136, 59–86.

Costain, J. K., Domoracki, W. J., Coruh, C., 1990. Processing and preliminary interpretation of Bottle Lake seismic reflection data. Maine Geological Survey Open-File Report 90-25d, 17 p.

Daphalapurkar, N. P., Ramesh, K. T., Graham-Brady, L., Molinari, J. F., 2011. Predicting variability in the dynamic failure strength of brittle materials considering pre-existing flaws. Journal of the Mechanics and Physics of Solids 59, 297–319.

Evans, J. P. , 1988. Deformation mechanisms in granitic rocks at shallow crustal levels. Journal of Structural Geology 10, 437–443.

Doan, M.-L., d'Hour, V., 2012. Effect of initial damage on rock pulverization along faults. Journal of Structural Geology 45, 113–124.

Doan, M.-L., Gary, G., 2009. Rock pulverization at high strain rate near the San Andreas fault. Nature Geoscience 2, 709–712.

Doll, W. E., Domoracki, W. J., Costain, J. K., Coruh, C., Ludman, A., Hopeck, J. T., 1996. Seismic reflection evidence for the evolution of a transcurrent fault system. The Norumbega fault zone, Maine. Geology 24, 251–254.

Dor, O., Ben-Zion, Y., Rockwell, T. K., Brune, J., 2006a. Pulverized rocks in the Mojave section of the San Andreas Fault zone. Earth and Planetary Science Letters 245, 642–654.

Dor, O., Chester, J. S., Ben-Zion, Y., Brune, J., Rockwell, T. K., 2009. Characterization of damage in sandstones along the Mojave section of the San Andreas Fault: Implications for the shallow extent of damage generation. Pure and Applied Geophysics 166, 1747–1773.

Dor, O., Rockwell, T. K., Ben-Zion, Y., 2006b. Geological observations of damage asymmetry in the structure of the San Jacinto, San Andreas, and Punchbowl Faults in southern California: A possible indicator for preferred rupture propagation direction. Pure and Applied Geophysics, 163, 301–349.

Dor, O., Yildirim, C., Rockwell, T. K., Ben-Zion, Y., Emre, O., Sisk, M., Duman, T. Y., 2008. Geological and geomorphologic asymmetry across the rupture zones of the 1943 and 1944 earthquakes on the North Anatolian Fault: possible signals for preferred earthquake propagation direction. Geophysical Journal International 173, 483–504.

Fonderiest, M., Aretusini, S., Di Toro, G., Smith, S. A. F., 2015. Fracturing and rock pulverization along an exhumed seismogenic fault zone in dolostones: The Foiana Fault Zone (Southern Alps, Italy). Tectonophysics 654, 56–74.

Gapais, D., 1989. Shear structures within deformed granites: mechanical and thermal indications. Geology 17, 1144–1147.

Gleason, G. C., Tullis, J., 1995. A flow law for dislocation creep of quartz aggregates determined with the molten salt cell. Tectonophysics 247, 1–23.

Goldstein, A., Hepburn, J. C., 1999. Possible correlations of the Norumbega fault system with faults in southeastern New England, in Ludman, A. and West, D.P., Jr., eds., The Norumbega Fault System of the Northern Appalachians: Geological Society of America Special Paper 331, p. 73–84.

Grifith, W. A., Nielsen, S., Di Toro, G., Smith, S. A. F., 2010. Rough faults, distributed weakening, and off-fault deformation. Journal of Geophysical Research 115, B08409, doi:10.1029/2009JB006925.

Gtöze, J., Plötze, M., Habermann, D., 2001. Origin, spectral characteristics and practical applications of the cathodoluminescence (CL) or quartz–a review. Mineralogy and Petrology 71, 225–250.

Handy, M. R., Brun, J.-P., 2004. Seismicity, structure and strength of the continental lithosphere. Earth and Planetary Science Letters 223, 427–441.

Hatcher, R. D., Jr., 2010, The Appalachian orogen: A brief summary. In: Tollo, R. P. Bartholomew, M. J., Hibbard, J. P., Karabinos, P. M. (Eds.), From Rodinia to Pangea: The lithotectonic record of the Appalachian region: Boulder, Colorado, Geological Society of America Memoir 206, p. 1–19.

Huang, R., Audétat, A., 2012. The titanium-in-quartz (TitaniQ) thermobarometer: a critical examination and re-calibration. Geochimica Cosmochimica Acta 84, 75–89

Healy, D., Rizzo, R. E., Cornwell, D. G., Farrell, N. J. C., Watkins, H., Timms, N. E., Gomez Rivas, E., Smith, M., 2017. FracPaQ: A MATLAB toolbox for the quantification of fracture patterns. Journal of Structural Geology 95, 1–16.

Hibbard, J. P., van Staal, C. R., Rankin, D. W., Williams, H., 2006. Lithotectonic map of the Appalachian orogen, Canada - United States of America. Geological Survey of Canada Map 02096A, 2 sheets, scale 1:1,500,000.

Hirth G., Teyssier, C., Dunlap, W. J., 2001. An evaluation of quartzite flow laws based on comparisons between experimentally and naturally deformed rocks. International Journal of Earth Sciences 90, 77–87.

Hirth G., Tullis, J., 1992. Dislocation creep regimes in quartz aggregates. Journal of Structural Geology 14, 145–160.

Hirth G., Tullis, J., 1994. The brittle-plastic transition in experimentally deformed quartz aggregates. Journal of Geophysical Research 99, 11,731–11,747.

Holdaway, M. J., 1971. Stability of andalusite and the aluminum silicate phase diagram. American Journal of Science 271, 97–131.

Kirkpatrick, J. D., Rowe, C. D., 2013. Disappearing ink: How pseudotachylytes are lost from the rock record. Journal of Structural Geology 52, 183–198.

Kruhl, J. H., 1996. Prism- and basal-plane parallel subgrain boundaries in quartz: a microstructural geothermobarometer. Journal of Metamorphic Geology, 14, 581–589.

Küster, M., Röller, K., Fischer, M., McConnel, V. S., Stöckhert, B., 2001. The record of episodic phase separation (H2O–CO2) in a hydrothermal system—quartz microstructures and fluid inclusions at Long Valley Exploratory Well. XVI ECROFI Faculdade de Ciências do Porto, Departamento de Geologia, Memória n°7, Porto, p. 245–248.

Leeman, W.P., MacRae, C.M., Wilson, N.C., Torpy, A., Lee, C.-TA., Student, J. J., Thomas, J. B., Vicenzi, E. P., 2012. Quantitative application of cathodoluminescence (CL) to natural quartz with application to geothermobarometry. Microscopy and Microanalysis 18, 1322–1341.

Lister, G. S., Snoke, A. W., 1984. S-C mylonites. Journal of Structural Geology 6, 617–638.

Ludman, A., 1998. Evolution of a transcurrent fault zone in shallow crustal metasedimentary rocks: The Norumbega fault zone, eastern Maine. Journal of Structural Geology 20, 93–107.

Ludman, A., Berry, H. N., IV, 2003. Bedrock Geology of the Calais 1:100,000 Quadrangle, Maine. Maine Geological Survey Open-File 03-97, scale 1:100,000.

Ludman, A., Lanzirotti, A., Lux, D., and Chunzeng, W., 1999. Constraints on timing and displacement of multiple shearing in the Norumbega fault system, eastern Maine. In: Ludman, A., West, D.P., Jr., (Eds.), The Norumbega Fault System of the Northern Appalachians. Geological Society of America Special Paper vol. 331, pp. 179–194.

Ludman, A., Wang, C., Gibbons, S., Idleman, B., Rasbury, T., 2000. Geometry and timing of multiple faulting events in the Kellyland fault zone (Norumbega fault system) in the Fletcher Peak-Waabassus Mountain area, eastern Maine. In: Yates, M., Lux, D., Kelley, J. (Eds.), Guidebook for Field Trips in Coastal and East-Central Maine. Guidebook-New England Intercollegiate Geological Conference, vol. 92, pp. 1 –22.

Ludman, A., West, D. P., Jr., 1999. Preface to: Norumbega Fault System of the Northern Appalachians In: Ludman, A. and West, D.P., Jr., (Eds.), The Norumbega Fault System of the Northern Appalachians. Geological Society of America Special Paper vol. 331, pp. v–xii.

Melosh, B. L., Rowe, C. D., Smit, L., Groenewald, C., Lambert, C. W., Macey, P., 2014. Snap, Crackle, Pop: Dilational fault breccias record seismic slip below the brittle–plastic transition. Earth and Planetary Science Letters 403, 432–445.

Mills, S. G., Gerbi, C., Marsh, J. H., Yates, M. G., Seaman, S. J., White, J. C., 2017. Tectonic and chemical implications of cathodoluminescent microstructures in quartz, Parry Sound domain, Ontario, Canada. Canadian Journal of Earth Science 54, 677–692.

Mitchell, T. M., Ben-Zion, Y., Shimamoto, T., 2011. Pulverized fault rocks and damage zone asymmetry along the Arima-Takatsuki Tectonic Line, Japan. Earth and Planetary Science Letters 308, 284–297.

Muto, J., Nakatani, T., Nishikawa, O., Nagahama, H., 2015. Fractal particle size distribution of pulverized fault rocks as a function of distance from the fault core. Geophysical Research Letters 42, 3811–3819.

Nelis, M. K., Mosher, S., 1998. Brittle deformation of granite. In: Snoke, A. W., Tullis, J., Todd, V. R., (Eds.), Fault-related rocks: A photographic atlas. Princeton University Press, Princeton, New Jersy, pp. 22–27.

New Brunswick Department of Natural Resources and Energy, 2000. Bedrock Geology of New Brunswick. Minerals and Energy Division Map NR-1 (2000 Edition), scale 1:500,000.

Osberg, P.H., Hussey II, A.M., Boone, G.M., 1985. Bedrock geologic map of Maine. Augusta, Maine Geologic Survey, scale 1:500,000.

Passchier, C. W., 1982. Pseudotachylyte and the development of ultramylonite bands in the Saint-Barthelemy Massif, French Pyrenees. Journal of Structural Geology 4, 69–79.

Pattison, D. R., 1992. Stability of andalusite and sillimanite and the Al2SiO5 triple point: Constraints from the Ballachulish Aureole, Scotland. Journal of Geology 100, 423–446.

Price, N. A., Johnson, S. E., Gerbi, C. C., West, D. P., Jr., 2012. Identifying deformed pseudotachylyte and its influence on the strength and evolution of a crustal shear zone at the base of the seismogenic zone. Tectonophysics 518-521, 63–83.

Reches, Z., Dewers, T. A., 2005. Gouge formation by dynamic pulverization. Earth and Planetary Science Letters 235, 361–374.

Rempe, M., Mitchell, T., Renner, J., Nippress, S., Ben-Zion, Y., Rockwell, T., 2013. Damage and seismic velocity structure of pulverized rocks near the San Andreas Fault. Journal of Geophysical Research: Solid Earth 118, 2813–2831, doi:10.1002/jgrb.50184.

Riley, D. N., 2004. Granites, orogeny, and the Deblois pluton complex in eastern Maine, USA. Ph.D. dissertation, Ohio State University, 546 pp.

Robinson, P., Tucker, R. D., Bradley, D., Berry, H. N., Osberg, P. H., 1998. Paleozoic orogens in New England, USA. Geologiska Föreningens i Stockholm Förhandlingar 120, 119–148.

Rockwell, T., Sisk, M., Girty, G., Dor, O., Wechsler, N., Ben-Zion, Y., 2009. Chemical and physical characteristics of pulverized Tejon Lookout Granite adjacent to the San Andreas and Garlock Faults: Implications for earthquake physics. Pure and Applied Geophysics 166, 1725–1746.

Rowe, C. D., Griffith, W. A., 2015. Do faults preserve a record of seismic slip: A second opinion. Journal of Structural Geology 78, 1–26.

Sibson, R. H., 1977. Fault rocks and fault mechanisms. Journal of the Geological Society, London 133, 191–213.

Sibson, R. H., 1986, Brecciation processes in fault zones: Inference from earthquake rupturing. Pure and Applied Geophysics 124, 159–175.

Simpson, C., 1985. Deformation of granitic rocks across the brittle-to-ductile transition. Journal of Structural Geology 7, 503–511.

Spear, F. S., 1993. Metamorphic phase equilibria and pressure-temperature-time paths. Mineralogical Society of America, Washington D.C., 799 pp.

Spear, F. S., Cheney, J. T., 1989. A petrogenetic grid for pelitic schists in the system SiO_2 - Al_2O_3 - FeO - MgO - K_2O - H_2O. Contributions to mineralogy and petrology 101, 149–164.

Spear, F. S., Wark, D. A., 2009. Cathodoluminescence imaging and titanium thermometry in metamorphic quartz. Journal of metamorphic geology 27, 187–205.

Spray, J. G., 2010. Frictional melting processes in planetary materials: From hypervelocity impact to earthquakes. Annual Reviews in Earth and Planetary Science 38, 221–254.

Stipp, M., Stünitz, H., Heilbronner, R., Schmid, S. M., 2002. Dynamic Recrystallization of quartz: Correlation between Natural and Experimental Conditions. In: de Meer, S., Drury, M.R., de Bresser, J.H.P., Pennock, G.M. (Eds.), Deformation Mechanisms, Rheology and Tectonics: Current Status and Future Perspectives. Geological Society, London, Special Publication 20, 171–190.

Sullivan, W. A., Boyd, A. S., Monz, M. E., 2013. Strain localization in homogeneous granite near the brittle-ductile transition: A case study of the Kellyland fault zone, Maine, USA. Journal of Structural Geology 56, 70–88.

Sullivan, W. A., Monz, M. E., 2016. Rheologic evolution of low-grade metasedimentary rocks and granite across a large strike-slip fault zone: A case study of the Kellyland fault zone, Maine, USA. Journal of Structural Geology 86, 13–31.

Thomas, J. B., Watson, E. B., Spear, F. S., Shemella, F. S., Nayak, S. K., Lanzirotti, A., 2010. TitaniQ under pressure: the effect of pressure and temperature on the solubility of Ti in quartz. Contributions to Mineralogy and Petrology 160, 743–759.

Thomas, J. B., Watson, E. B., Spear, F. S., Wark, D. A., 2015. TitaniQ recrystallized: experimental confirmation of the original Ti-in-quartz calibrations. Contributions to Mineralogy and Petrology 169:27, doi:10.1007/s00410-015-1120-0.

Trepmann, C. A., Hsu, C., Hentschel, F., Döhler, K., Schneider, C., Wichmann, V., 2017, Recrystallization of quartz after low-temperature plasticity—The record of stress relaxation below the seismogenic zone. Journal of Structural Geology 95, 77–92.

Trepmann, C. A., Stöckhert, B., 2013. Short wavelength undulatory extinction in quartz recording coseismic deformation in the middle crust—an experimental study. Solid Earth 4, 263–276.

Trepmann, C. A., Stöckhert, B., Dorner, D., Moghadam, R., H., Küster, M., Röller, K., 2007. Simulating coseismic deformation of quartz in the middle crust and fabric evolution during postseismic stress relaxation—An experimental study. Tectonophysics 442, 83–104.

Tullis, J., 2002. Deformation of granitic rocks: Experimental studies and natural examples. In: Karato, S., Wenk, H. (Eds.), Plastic deformation of minerals and rocks. Reviews in Mineralogy and Geochemistry, vol. 51, pp. 51–95.

Tullis, J., Yund, R. A., 1987. Transition from cataclastic flow to dislocation creep of feldspar: Mechanisms and microstructures. Geology 15, 606–609.

Wang, C., 2007. Bedrock Geology of the Fletcher Peak 7.5' Quadrangle, Maine. Maine Geological Survey Open File 07-143, scale 1:24,000, 16 pp.

Wang, C., Ludman, A., 2004. Deformation conditions, kinematics, and displacement history of shallow crustal ductile shearing in the Norumbega fault system in the Northern Appalachians, eastern Maine. Tectonophysics 384, 129–148.

Wark, D. A., Watson, E. B., 2006. The TitaniQ: a titanium-in-quartz geothermometer. Contributions to Mineralogy and Petrology 152, 743–754.

Wechsler, N., Allen, E. E., Rockwell, T. K., Girty, G., Chester, J. S., Ben-Zion, Y., 2011. Characterization of pulverized granitoids in a shallow core along the San Andreas Fault, Littlerock, CA. Geophysical Journal International 186, 401–417.

West, D. P., Beal, H. M., Grover, T. W., 2003. Silurian deformation and metamorphism of Ordovician arc rocks of the Casco Bay Group, south-central Maine. Canadian Journal of Earth Sciences 40, 887–905.

Whearty, J. J., Rockwell, T. K., Girty, G. H., in press. Incipient pulverization at shallow burial depths along the San Jacinto fault, southern California. In: Thomas, M.Y., Mitchell, T.M., and Bhat, H.S. (Eds.), Fault zone dynamic processes: Evolution of fault properties during seismic rupture. Geophysical Monograph 227, John Wiley & Sons, Inc.

White, S., 1976. The Effects of Strain on the Microstructures, Fabrics, and Deformation Mechanisms in Quartzites. Philosophical Transactions of the Royal Society, London 283, 69–86.

Wilson, B., Dewers, T., Reches, Z., Brune, J., 2005. Particle size and energetics of gouge from earthquake rupture zones. Nature 434, 749–752.

Xia, K., Yao, W., 2015. Dynamic rock tests using split Hopkinson (Kolsky) bar system—a review. Journal of Rock Mechanics and Geotechnical Engineering 7, 27–59.

Xu, S., Ben-Zion, Y., 2017. Theoretical constraints on dynamic pulverization of fault zone rocks. Geophysical Journal International 209, 282–296.

Yuan, F., Prakash, V., Tullis, T., 2011. Origin of pulverized rocks during earthquake fault rupture. Journal of Geophysical Research 116, B06309, doi:10.1029/2010JB007721.

Figure captions

Figure 1. (A) Simplified bedrock geologic map of Maine, USA, showing the Norumbega fault system and correlative dextral strike-slip faults. DG = Deblois granite and KFZ = Kellyland fault zone. Compiled from: Osberg et al., 1985; Goldstein and Hepburn, 1999; New Brunswick Department of Resources and Energy, 2000; Ludman and Berry, 2003; West et al., 2003; Wang and Ludman, 2004; and Hibbard et al., 2006. (B) Geologic map of the study area showing strain facies in the KFZ and sample locations. Modified from Ludman and Berry, 2003; Wang, 2007; and Sullivan et al., 2013. Exact field location of KL51 shown in Figure 2 of Sullivan et al. (2013).

Figure 2. (A) Partial outcrop map of station KL40 showing sample locations and the mylonite/ultramylonite zone. (B) Photograph of granite with no foliation at station KL40. U.S. penny for scale is 1.9 cm in diameter. (C) Photograph of foliated-granite at station KL110 just outside the localized-shear-zone domain (Fig. 1B). Note the difference in the mm- to cm-scale weathering pattern of feldspars between this outcrop and that shown in B. U.S. penny for scale.

Figure 3. Images of sample KL40-2B. (A) Full-thin-section scan under cross-polarized light showing fragmented quartz, optically continuous microcline, mylonitic shear zone, and shear fracture. (B) Cross-polarized-light image of quartz and microcline cut by the shear fracture. Arrows point out healed fractures marked by bands of neoblasts. (C) Color-CL image of optically continuous microcline. Arrows highlight CL-dark healed fractures. (D) Map of fractures and recrystallized zones in the microcline grain in (C) and rose diagram showing fracture orientations compiled from the map. (E) Matched color-CL and BSE images of a dilational fracture in microcline. The oval and polygon highlight CL-bright island grains in the fracture fill. The rectangle highlights a later biotite + quartz-filled fracture cutting the K-feldspar filled fracture.

Arrows mark other cross-cutting healed fractures. Mineral abbreviations are: Bt = biotite, Kfs = K-feldspar, Plg = plagioclase, Qtz = quartz, and Umyl is ultramylonite matrix. For references to color, see the online version of this manuscript.

Figure 4. Images of KL40-8. (A) Full-thin-section scan under cross-polarized light showing the primary igneous grain shapes, fragmented quartz, optically continuous microcline, and small shear fracture. (B) Cross-polarized-light image of quartz. Arrows highlight healed fractures marked by bands of neoblasts. (C) Color-CL image of quartz. Arrows highlight healed fractures marked by CL-dark bands. (D) BSE image of a plagioclase grain hosted in quartz. Note the planar network of biotite-filled fractures along albite-twin planes. (E) Color-CL image of optically continuous microcline. Arrows highlight healed fractures marked by CL-dark bands. (F) Map of fractures and recrystallized zones in the microcline grain in (E) and rose diagram showing fracture orientations compiled from the map. (G) Matched color-CL and BSE images of optically continuous microcline. Oval highlights cross-cutting, K-feldspar-filled dilational fractures. Arrows and rectangle highlight additional healed fractures. (H) Map of fractures and recrystallized zones in the microcline grain in (G) and rose diagram showing fracture orientations compiled from the map. Mineral abbreviations are the same as in Figure 3. For references to color, see the online version of this manuscript.

Figure 5. Maps of fractures and recrystallized zones in two optically continuous microcline grains in sample KL115 and a single grain in KL109-B. The rose diagrams accompanying each map show the orientations of fractures compiled from the unit circles centered in the map areas relative to the mesoscopic foliation in each sample.

Figure 6. Images of undeformed granite sample KL51 collected ~4.9 km across strike from the KFZ (See Figure 2 of Sullivan et al., 2013 for sample location). (A) Full-thin-section scan under cross-polarized light showing the primary grain shapes and igneous texture. Note the rapakivi

overgrowth of plagioclase on microcline near the center of the image and the tartan twinning and exsolution lamellae in microcline. (B) Color-CL image of quartz. The thin, dark bands are optically visible grain boundaries. Note the absence of healed fractures. (C) Cross-polarized-light image of a microcline grain hosting subhedral quartz inclusions. Note the tartan twinning, perthitic exsolution lamellae, and absence of healed fractures. (D) Color-CL and backscattered-electron images of the same field of view in a microcline grain. Note the perthitic exsolution lamellae visible in both images, the tartan twinning visible in the CL image, and the absence of healed fractures. Cracks visible in the images are from sample preparation. Mineral abbreviations are the same as in Figure 3. For references to color, see the online version of this manuscript.

Figure 7. Images of KL41 and KL110. (A) Outcrop photo of granite at KL41. U.S. Penny for scale. (B) Full-thin-section scan of sample KL41 under cross-polarized light showing the primary grain shapes, fragmented quartz, and optically continuous microcline. The rounded rectangle highlights quartz with few or no fractures as described in the text. (C) Color-CL image of fragmented quartz in KL41. Arrows highlight healed fractures marked by CL-dark bands. (D) Color-CL image of microcline grain in KL41. Arrows highlight cross-cutting healed fractures marked by CL-dark bands. (E) Full-thin-section scan of sample KL110 under cross-polarized light showing dynamically recrystallized quartz and the C and S foliations. Arrows mark healed dilational fractures in microcline. (F) Color-CL image of dynamically recrystallized quartz in KL110. Arrow highlights a healed fracture in a relict grain. (G) Color-CL image of optically continuous microcline in KL110. Arrows highlight healed fractures marked by CL-dark bands. Mineral abbreviations are the same as in Figure 3. For references to color, see the online version of this manuscript.

*Figure 01

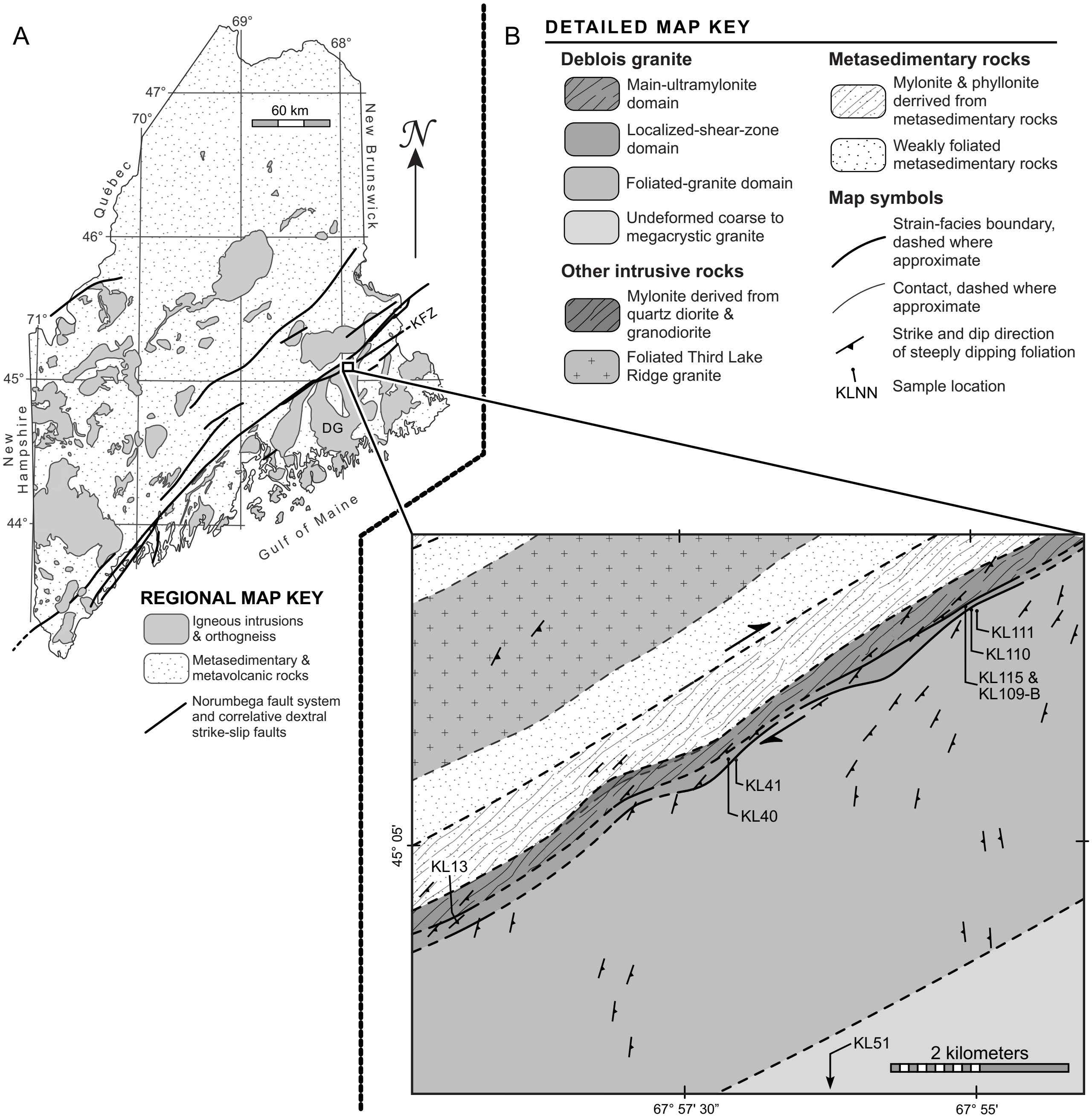
A
69°
68°
47°
70°
60 km
Québec
New Brunswick
46°
71°
KFZ
45°
New Hampshire
DG
44°
Gulf of Maine
REGIONAL MAP KEY
Igneous intrusions & orthogneiss
Metasedimentary & metavolcanic rocks
Norumbega fault system and correlative dextral strike-slip faults
B
DETAILED MAP KEY
Deblois granite
Main-ultramylonite domain
Localized-shear-zone domain
Foliated-granite domain
Undeformed coarse to megacrystic granite
Other intrusive rocks
Mylonite derived from quartz diorite & granodiorite
Foliated Third Lake Ridge granite
Metasedimentary rocks
Mylonite & phyllonite derrived from metasedimentary rocks
Weakly foliated metasedimentary rocks
Map symbols
Strain-facies boundary, dashed where approximate
Contact, dashed where approximate
Strike and dip direction of steeply dipping foliation
KLNN
Sample location
KL111
KL110
KL115 & KL109-B
KL41
KL40
45° 05'
KL13
KL51
2 kilometers
67° 57' 30"
67° 55'

***Figure 02**

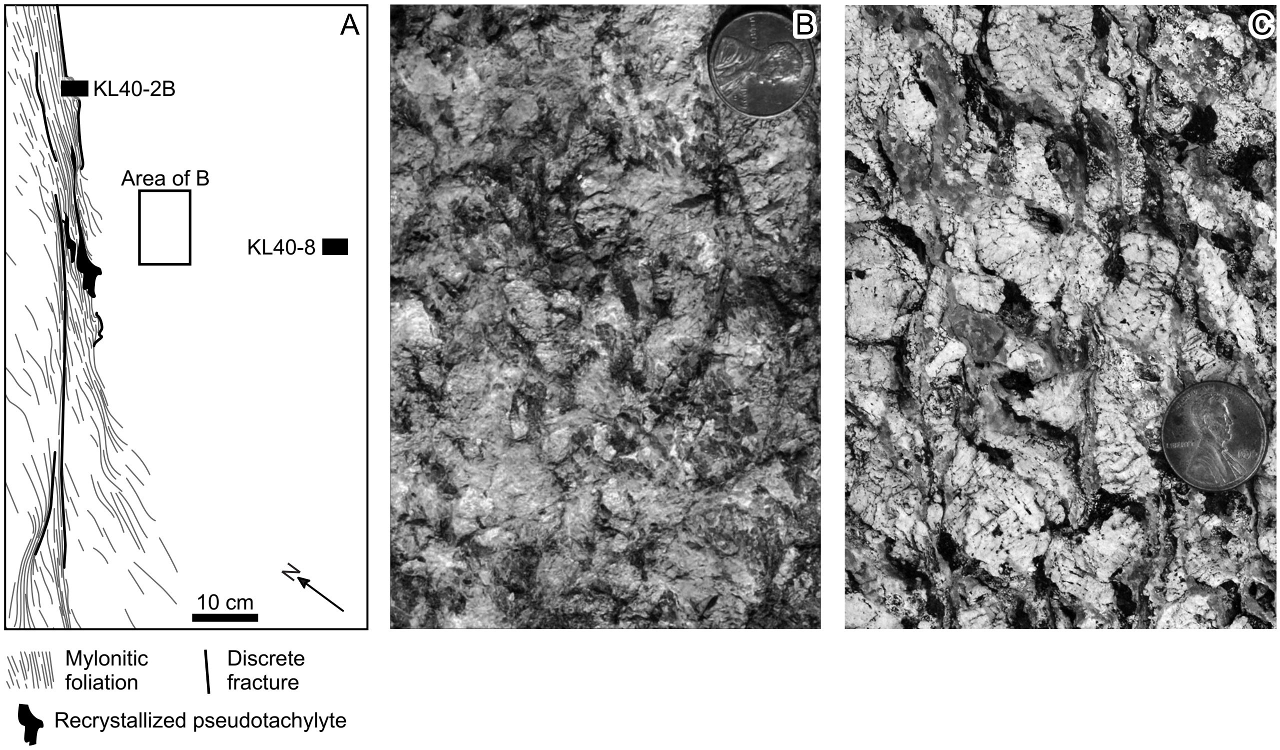
A
KL40-2B
Area of B
KL40-8
N
10 cm
B
C
Mylonitic foliation
Discrete fracture
Recrystallized pseudotachylyte

*Figure 03 color

Click here to download high resolution image

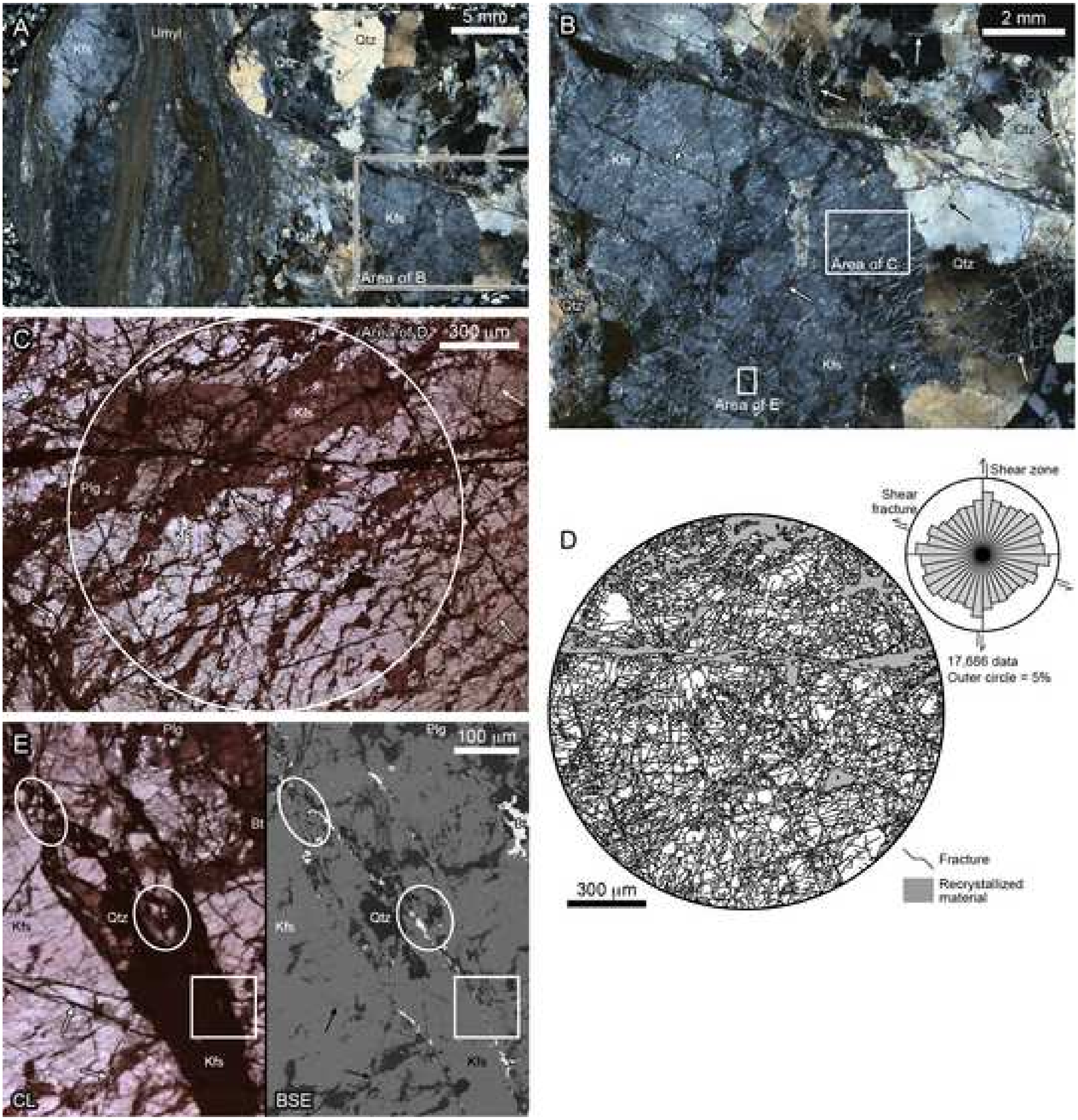

*Figure 03 gray scale
Click here to download high resolution image

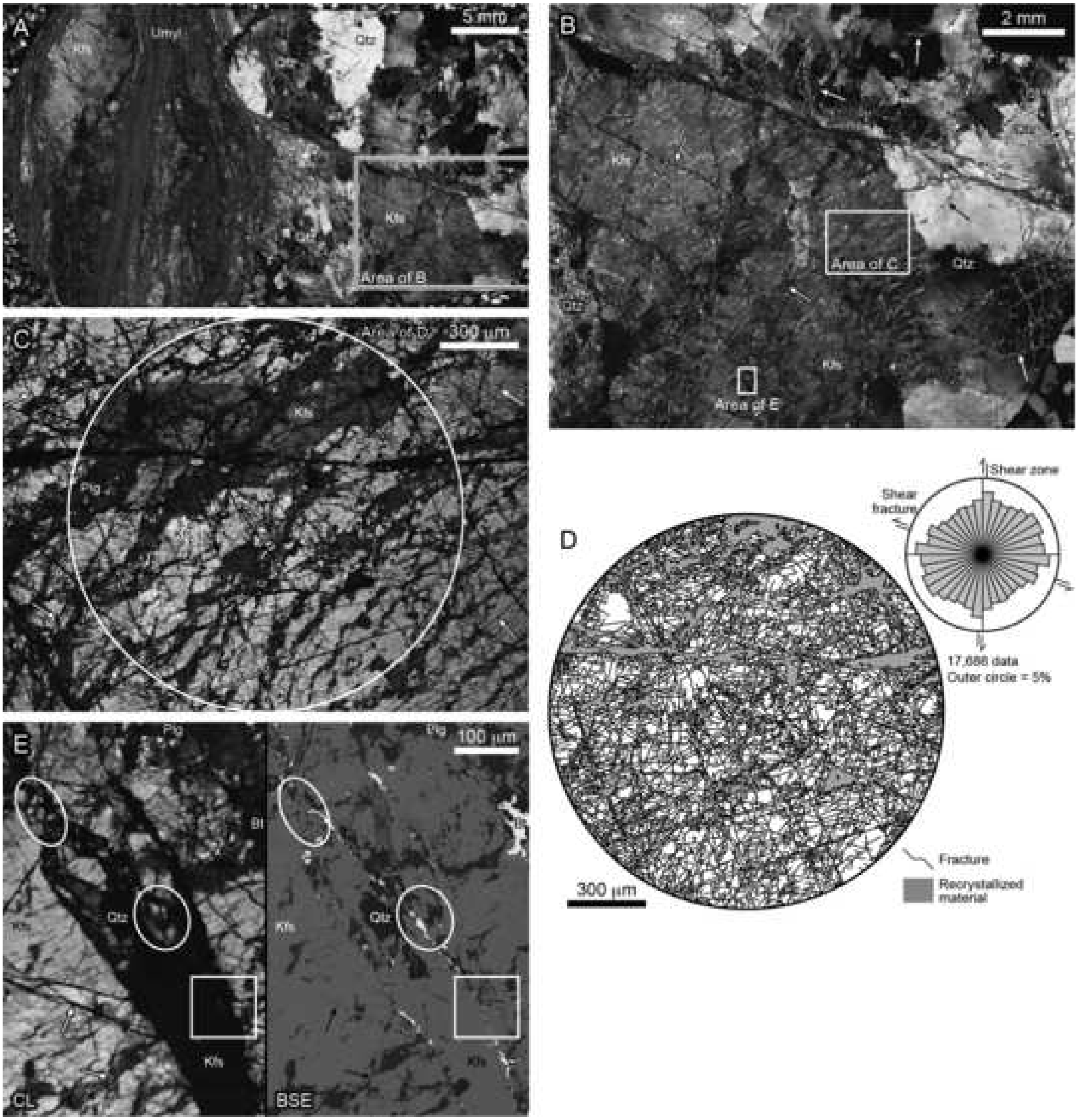

Figure 04 color

Click here to download high resolution image

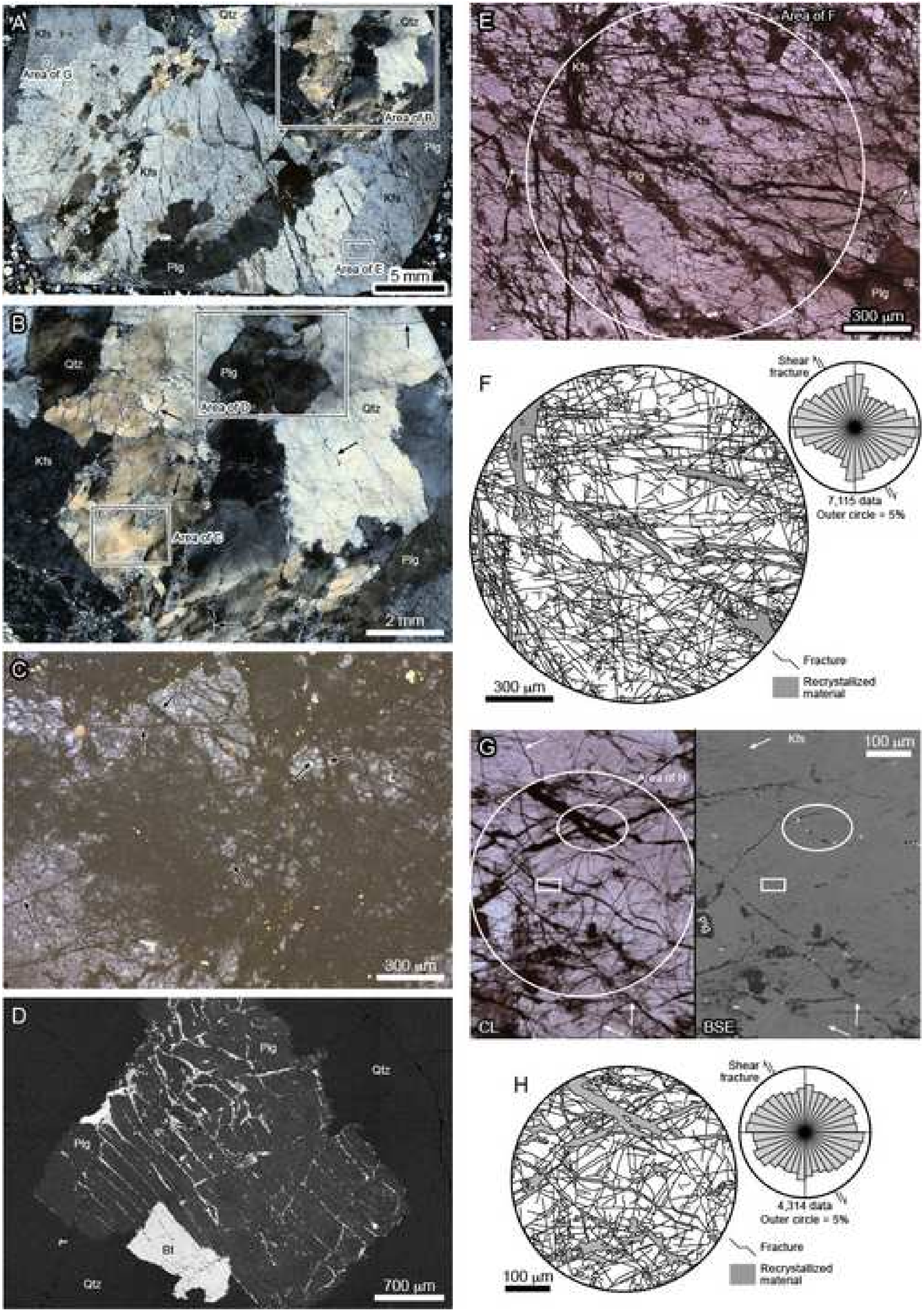

Figure 04 gray scale
Click here to download high resolution image

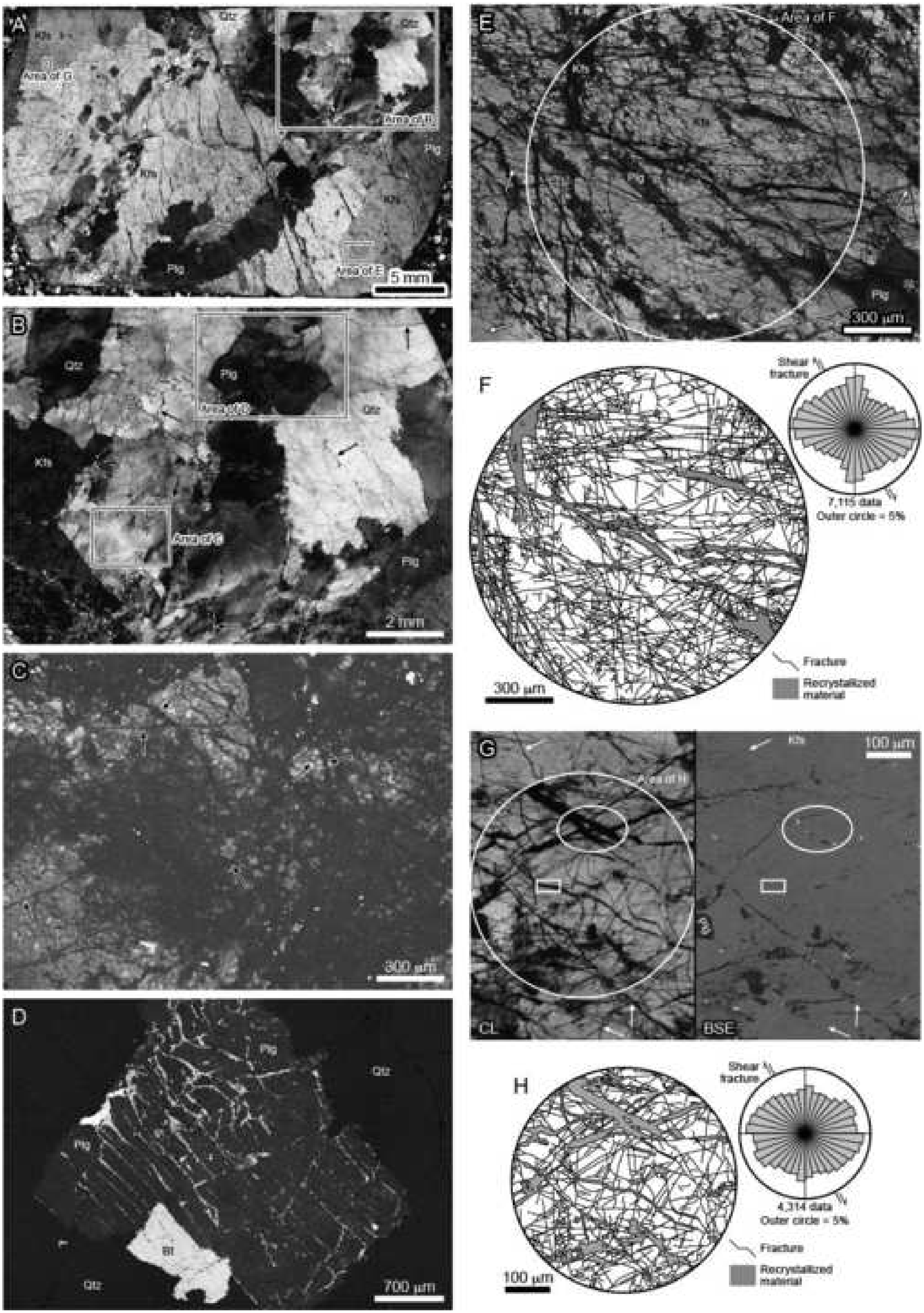

Figure 05

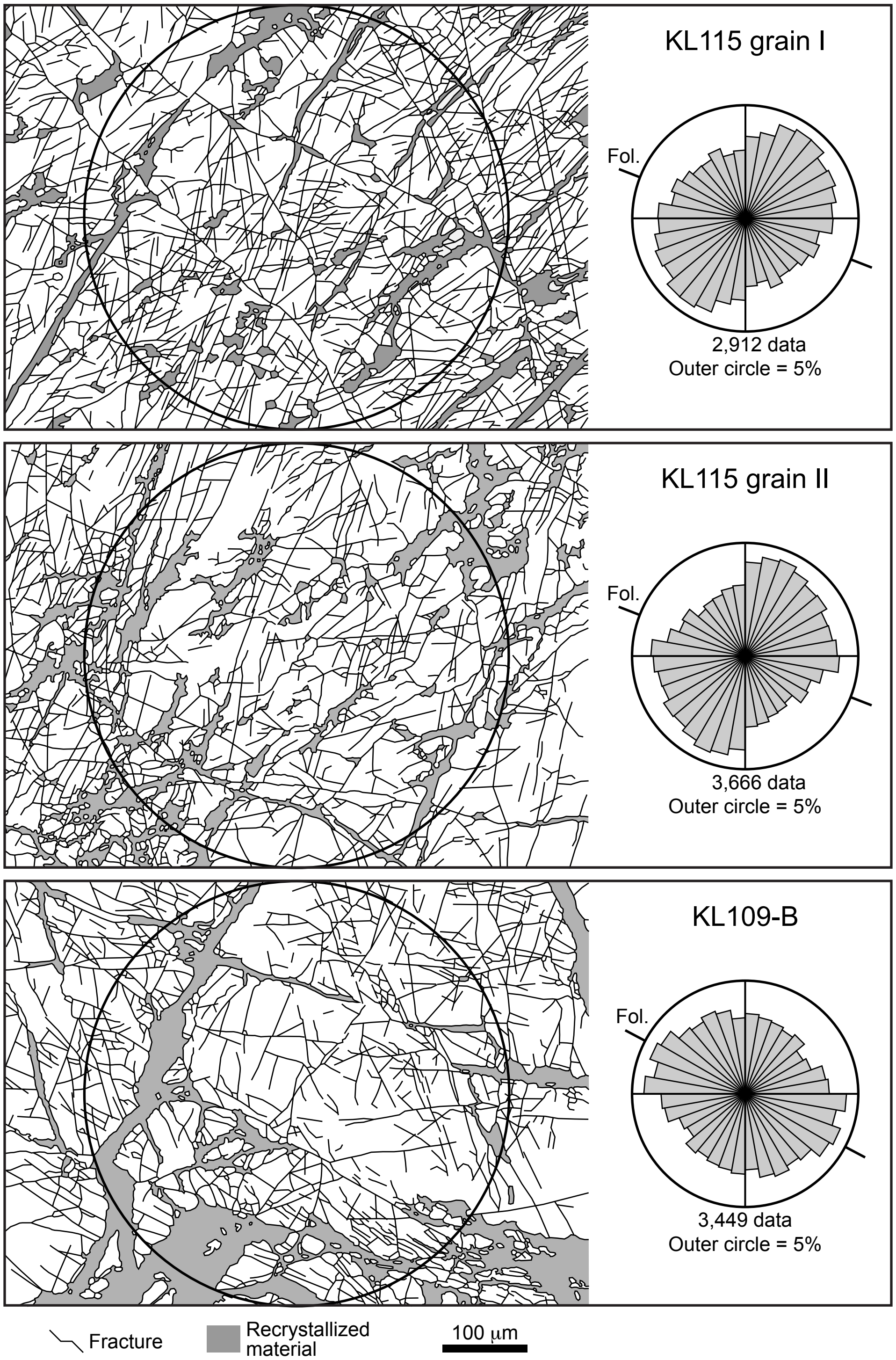
KL115 grain I
Fol.
2,912 data
Outer circle = 5%
KL115 grain II
Fol.
3,666 data
Outer circle = 5%
KL109-B
Fol.
3,449 data
Outer circle = 5%
Fracture
Recrystallized material
100 µm

*Figure 06 color
Click here to download high resolution image

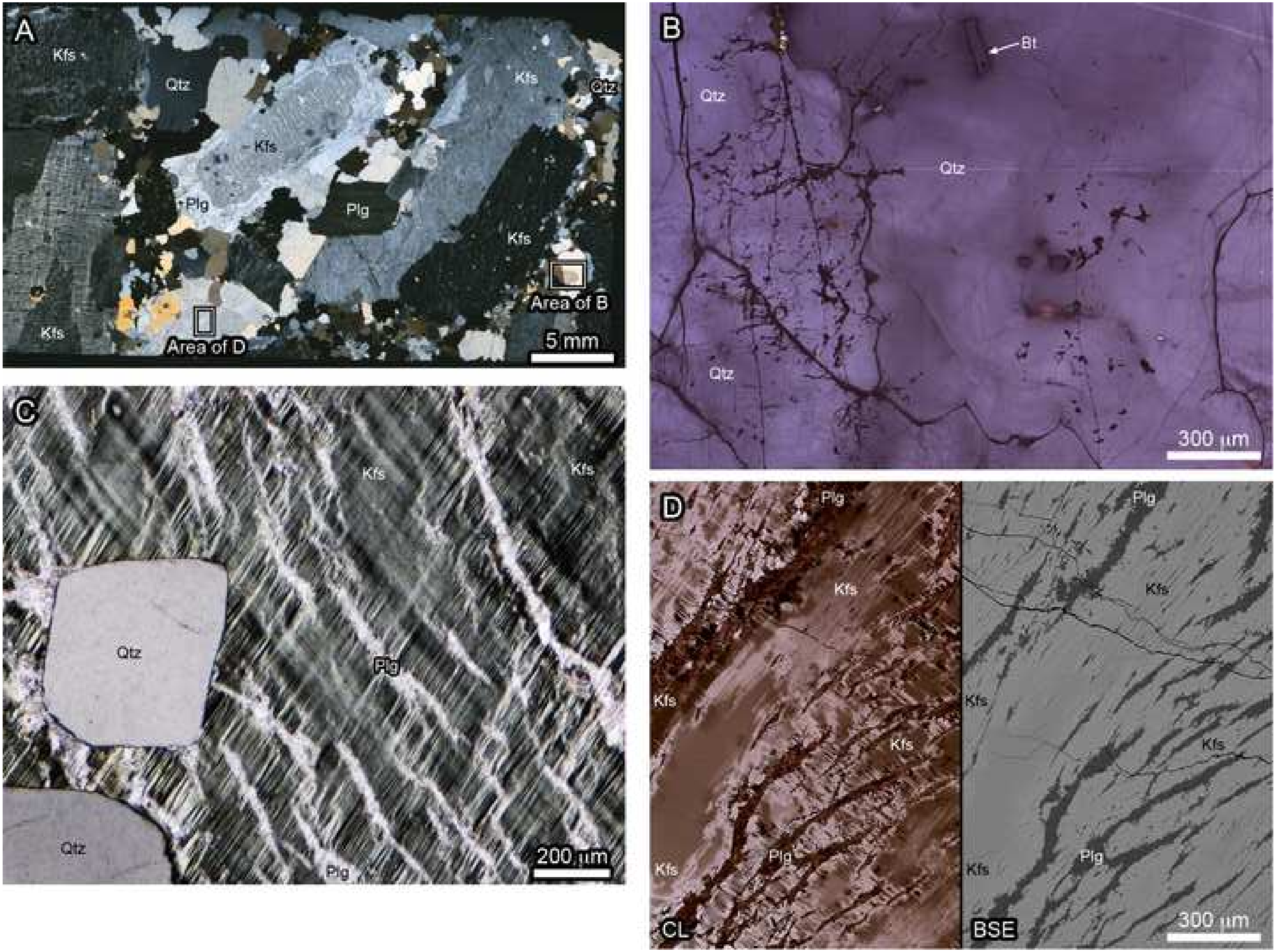

*Figure 06 gray scale
Click here to download high resolution image

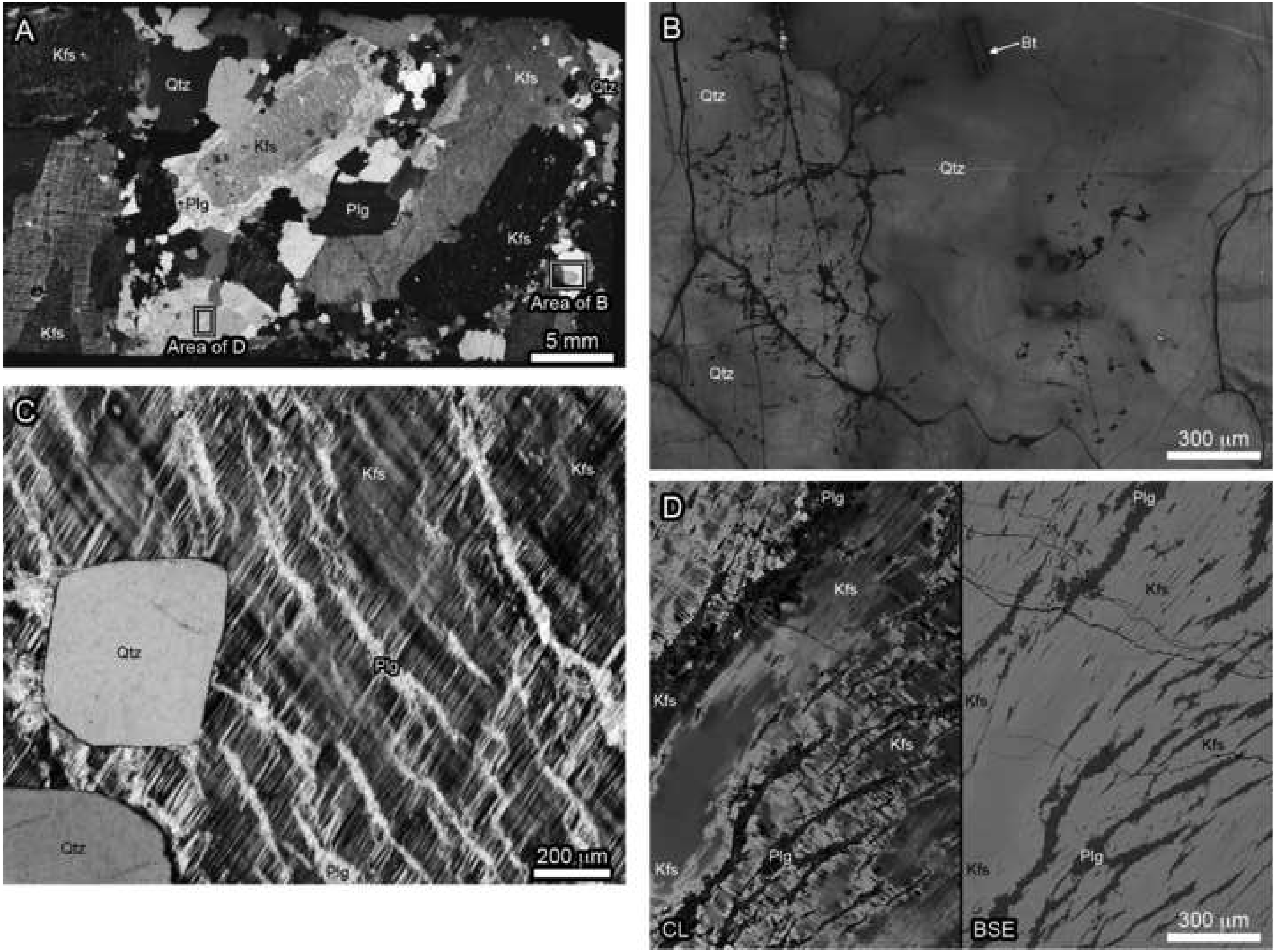

*Figure 07 color

Click here to download high resolution image

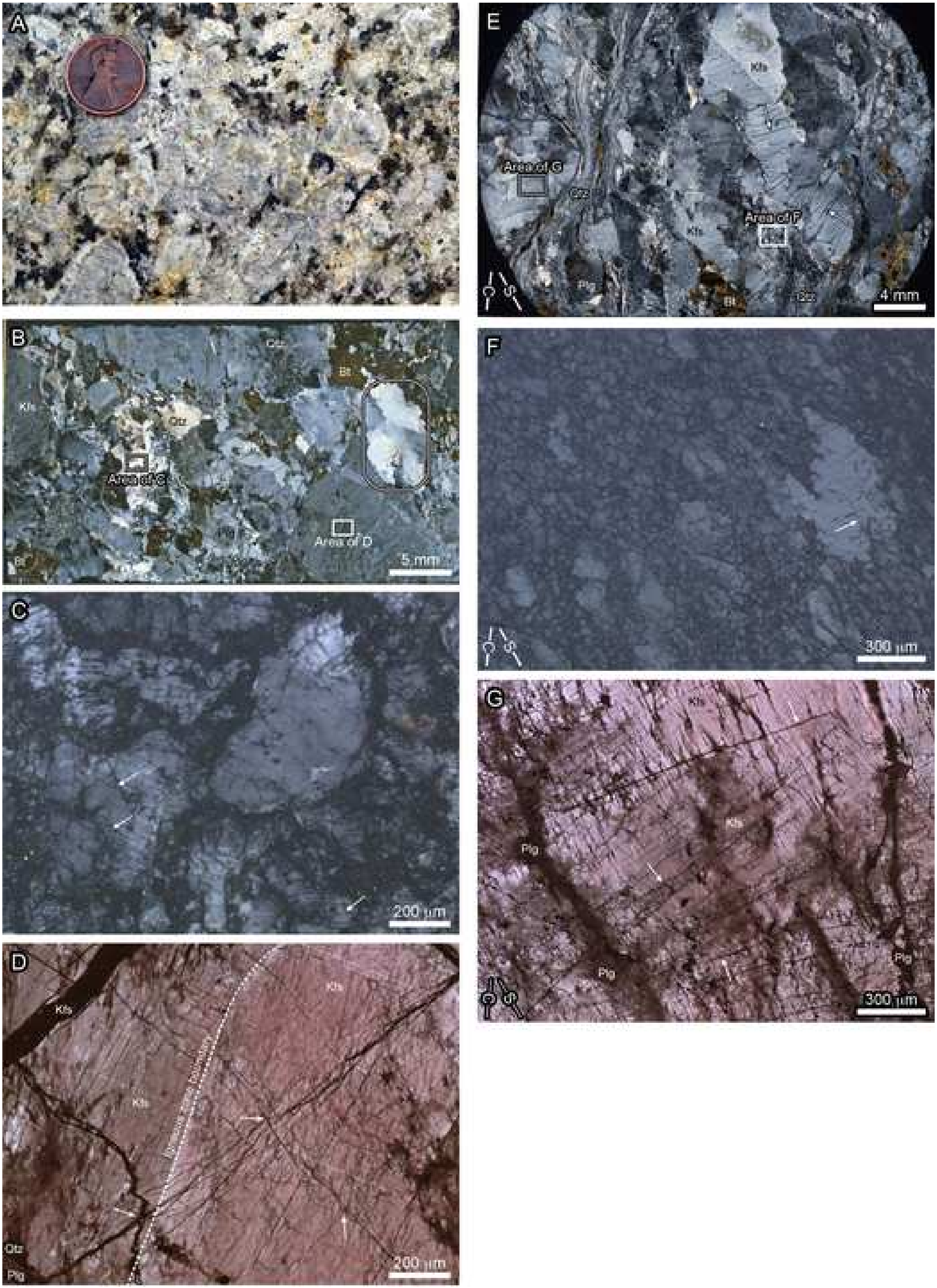

*Figure 07 gray scale

Click here to download high resolution image

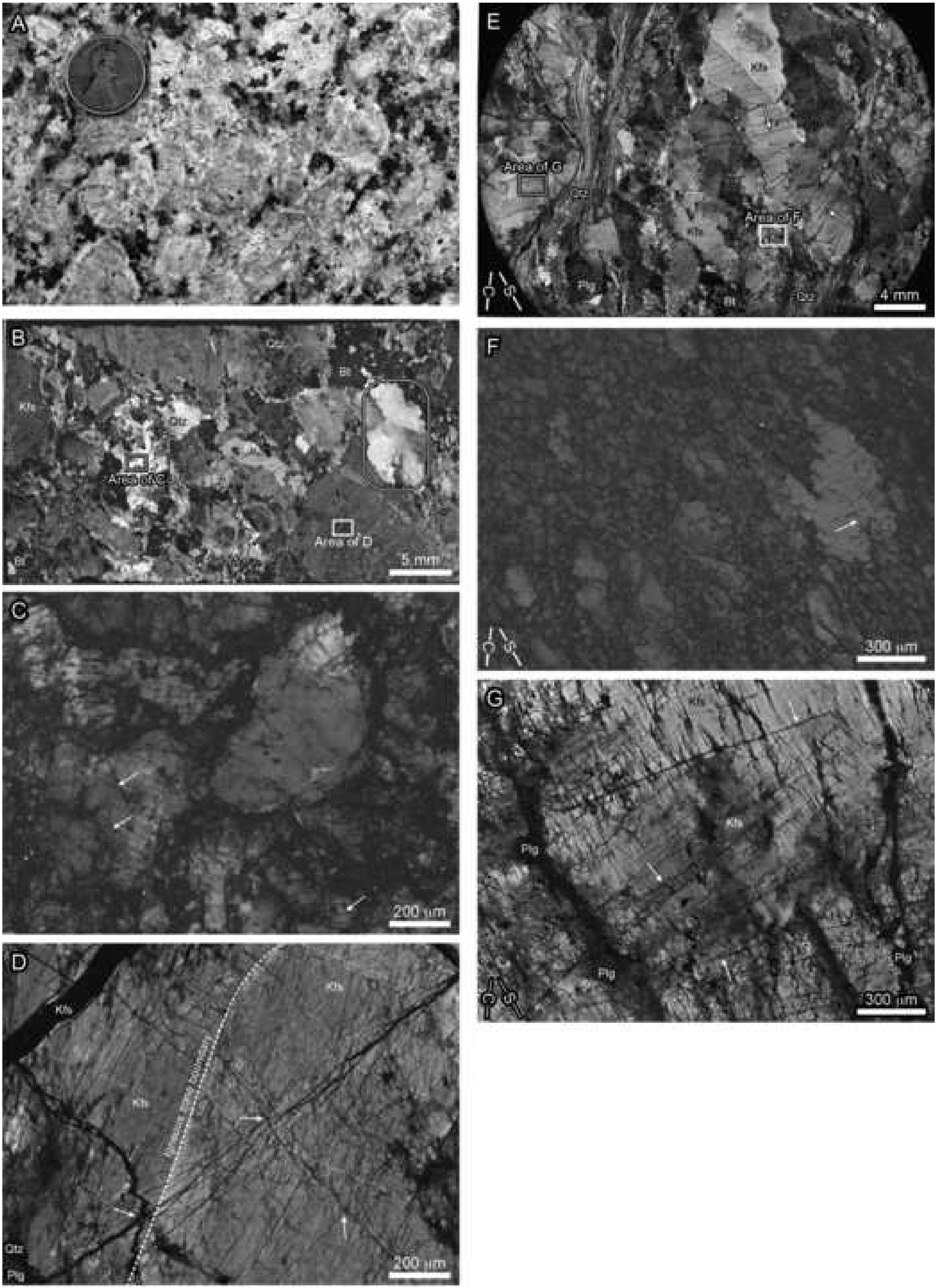

Table 1 revised

Table 1: Fracture-density measurements

Sample	Fracture map	Fracture density (mm/mm^2)	Fracture density (m/m^2)
KL40-2B	Fig. 3D	118	118,000
KL40-8	Fig. 4F	75	75,300
	Fig. 4H	130	130,000
KL115	Fig. 5, grain I	127	127,000
	Fig. 5, grain II	96	96,200
KL109-B	Fig. 5	103	103,000